Structural Characterization of Amorphous Silicon

Bianca Haberl

A thesis submitted for the degree of
Doctor of Philosophy
of
The Australian National University

December 2010

Chapter 1

Introduction

1.1 Order in Disorder: Structure in an Amorphous Network

Amorphous materials have been in use by human civilizations since the stone age when sharp tools were made from the volcanic glass obsidian [1, 2]. In the bronze age conventional glass became the first man-made amorphous material in Egypt [3, 4]. Specialized modern materials such as chalcogenide glasses, which have applications for data-storage [5], and diamond-like carbon (tetrahedral amorphous carbon), which is a widely used material for hard coatings [6, 7], continue the importance of amorphous structures. Finally, amorphous silicon (a-Si) in its hydrogenated form is a key electronic material for thin-film transistors [8] and photovoltaics [9] among many other applications. However, despite this widespread and longstanding use, understanding of the structure of amorphous materials has only emerged over the last century and much work still remains to be done.

The term 'amorphous' stems from ancient Greek and literally means 'without form'. However, for a-Si and many other amorphous solids this should not be taken literally, as they do contain a significant amount of structure. In fact, it is their structure which makes them interesting. Although amorphous materials lack the long-range order (LRO) of their crystalline counterparts, some order - or structure - remains due to the topological order caused by the chemical bonding of the atoms. Therefore, the theoretical approach to describe such amorphous materials is often based on this bonding with emphasis lying on the short-range order (SRO) [range up to $\sim$8 Å] rather than on the LRO used to describe crystalline materials. This makes them more challenging than crystalline materials from a scientific perspective. In order to describe this absence of periodicity and symmetry, Zachariasen introduced the model of a continuous random network (CRN) for glasses [10]. Therein, the atoms are linked by the same forces as present in crystals, but with tetrahedra building up to an aperiodic vitreous network. Thus, the only specific structural feature is the full four-fold coordination of each atom.

The structure of amorphous silicon has attracted particular interest over the recent decades [11–15] as it has been regarded as a model system of a covalently bonded CRN. The nature of the strong covalent Si-Si bonding does not allow for large deviations from the mean bond-length or bond-angle and its monatomic nature simplifies theoretical considerations. Therefore, it can be expected that the understanding of the structure of a-Si may also illuminate the structure of other covalently bonded amorphous materials such as tetrahedral amorphous carbon or amorphous germanium (a-Ge).

Amorphous silicon and amorphous germanium were first described as such a CRN by Polk in 1971 [11]. Polk built a CRN model from tetrahedral units consisting of a small, central section with four rods emanating from it and measured the mean bond-lengths and -angles. When scaled to the Si-Si bond-length, this model correlated well with the

structural properties of a-Si on the short-range order scale.

With the refinements of techniques greater insight has been gained into the order of a-Si, not only on the SRO-scale, but also into the realm beyond the SRO, the so-called medium-range order (MRO) [range of $\sim$1-3 nm]. These extensive studies have revealed significant deviations from the ideal CRN for most forms of a-Si. Intriguingly, also deviations *between* different forms of a-Si were observed with the structure depending on the formation method. A whole series of methods has been employed to make a-Si, ranging from chemical and physical vapour deposition techniques such as plasma-enhanced chemical vapour deposition and magnetron-sputtering to ion-implantation or quenching methods. However, to date it remains unclear to what extent variations in the production method of a-Si influences its structural order.

For example, ion-implanted and evaporated a-Si are reported to have very similar vibrational and thermodynamic properties [13, 16]. However, reverse Monte-Carlo modelling based on diffraction experiments performed on ion-implanted and evaporated a-Si found important differences between the two forms of a-Si: namely, ion-implanted a-Si was found to be somewhat more ordered with regions that are closer to the (ideal) regular tetrahedral form [17]. Furthermore, hybrid Metropolis Monte-Carlo modelling found significant differences between ion-implanted and porous a-Si with the dangling bonds congregating around the internal surfaces and with more ordered material between the pores in the latter case [18].

Another interesting feature of amorphous networks in general is that many of their properties depend not only on the formation mechanism, but also on the thermal history. For example, when subjected to annealing, a-Si formed by self-ion implantation undergoes 'structural relaxation' or short-range ordering to a form that is closer to an ideal CRN [13, 19]. This relaxation leads to changes in the vibrational, structural, thermodynamic and even mechanical properties [20–22]. Since the change in density is negligible ($<$0.1%) [23] the changes in the properties of ion-implanted a-Si are intrinsic to the amorphous network and not due to, for example, densification involving void removal as observed for deposited films [12].

Despite decades of research, there is still much to understand in terms of structural properties, especially the extent and nature of the order present within the network. This thesis addresses these issues. A range of different forms of a-Si prepared by a variety of methods including plasma-enhanced chemical vapour deposition (PECVD), magnetron-sputtering, quenching from the melt, ion-implantation and a pressure-induced structural collapse will be examined for their structural properties. A powerful combination of techniques will be employed such as nanoindentation, electron-energy-loss spectroscopy, quantitative electron diffraction, Raman microspectroscopy and fluctuation electron microscopy (FEM), which is a specialist transmission electron microscopy technique. The first two of these techniques give insight into the 'bulk' properties such as hardness and

mass density, whereas the other techniques yield information about the structural order, quantitative electron diffraction and Raman microspectroscopy on the SRO-scale and FEM on the MRO-scale. These structural properties of the different forms will be compared to each other, as not many comparative studies have been performed. Furthermore, the influence of the same thermal history on the various forms will be investigated as the influence of *ex situ* annealing has not been studied in depth, aside from the case of ion-implanted a-Si. Lastly, an entirely new form of a-Si created by a pressure-induced structural collapse, so-called pressure-induced (PI) a-Si, will be studied in detail. This form is a new pure form of a-Si and very little is known about any of its properties.

Not all of these forms of a-Si were studied with all experimental techniques, only the forms that allowed meaningful interpretation of the results. Thus, the aim of this work is to combine these studies to create an in-depth framework for the understanding of the structure of a-Si and possibly other covalently bonded amorphous materials.

In the remainder of this chapter, the nature of order on the SRO and MRO length-scales will be reviewed and the mechanism of structural relaxation is introduced in more detail. Thereafter, an insight into the high-pressure behaviour of a-Si and also c-Si will be given, as the mechanical properties are closely tied to this behaviour. Finally, the thesis structure will be outlined in detail.

1.1.1 Atomic Scale Order

Most early structural studies of a-Si concerned themselves only with the order on a length-scale up to ~8 Å. This section introduces this atomic scale order of a-Si.

The order on this length-scale can be represented by a radial-distribution function (RDF) or a pair-distribution function (PDF) [24]. The PDF shows the probability of finding one atom in a given distance from another atom at an arbitrary origin and averages over all atoms in the network. The RDF is the spherically-averaged PDF and contains similar information. Such an RDF is usually obtained by X-ray, neutron or electron diffraction methods, and has been investigated for a-Si since the late 1960s. Indeed, such an electron diffraction study on a-Si was able to confirm that a-Si is amorphous rather than microcrystalline for the first time [25]. An example of RDFs from as-implanted and relaxed (thermally annealed) implanted a-Si is shown in Fig. 1.1. The RDFs shown are taken from Laaziri *et al.* [14] and are the highest-resolution RDFs of pure a-Si in the existing literature.

Much structural information can be obtained from such RDFs. For instance, the position of the first peak in the RDF corresponds to the first-nearest neighbour distance (i.e. the mean bond-length) and the width is due to variations in the bond-lengths and thermal disorder. The coordination number is determined from the area under the first peak and the position of the second peak corresponds to the mean interatomic distance between

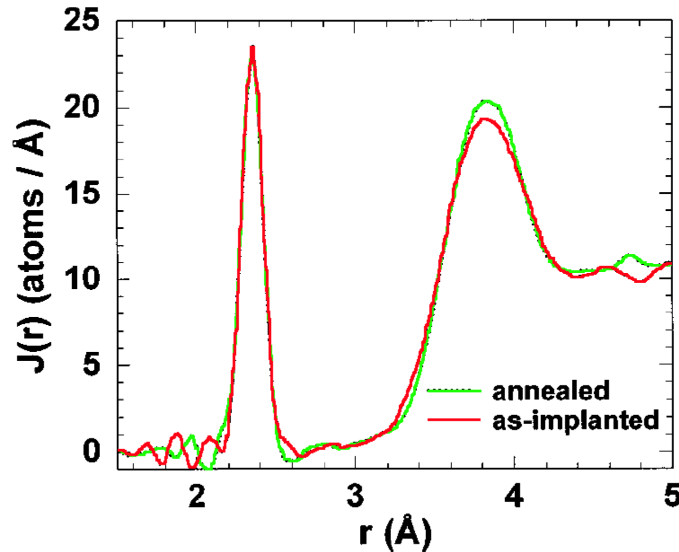

Figure 1.1: Radial distribution functions of annealed implanted (green line) and as-implanted (red line) a-Si obtained by X-ray diffraction by Laaziri *et al.* [14].

second-nearest neighbours and thus to the mean bond-angle.

Aside from the direct representation of the atomic pair-distribution, the vibrational properties of a-Si have also proven invaluable. Early calculations of the vibrational density of states of a-Si (and a-Ge) showed that the experimental Raman spectrum of a-Si correlates very well with the CRN model, but not with any smeared-out crystalline structures [26]. Furthermore, Raman microspectroscopy was found to be very sensitive to small changes in the SRO of the amorphous network [27, 28]. For example, the width of the transverse optic (TO)-like peak has been correlated to the bond-angle distortion by an empirical formula [29] (see Section 2.2.1 in the next chapter for details). This has been very useful when studying structural relaxation upon annealing as a significant decrease in peak width can be observed [13, 16, 28]. Examples of such Raman spectra taken from Roorda *et al.* [13] for as-implanted and annealed implanted a-Si are shown in Fig. 1.2. The respective peak half-widths of 43 cm^{-1} and 34 cm^{-1} are indicated in the figure. This correlates to a reduction in bond-angle distortion from 11.8° to 8.8° upon thermal annealing of ion-implanted a-Si.

In addition, it has been shown that the relative intensities of the other vibrational modes are sensitive to the intermediate-range order (IRO), which is the order beyond the first- and second-nearest neighbour [∼4-6 Å] [30]. The transverse acoustic (TA)-like peak in particular has been linked to the bond-bending modes and thus to the vibration of entire tetrahedra within the network [31]. Moreover, modelling of the vibrational density of states has indicated that a fully four-fold coordinated CRN is a realistic model for moderately disordered a-Si on this length-scale [30]. Therefore, the vibrational properties of a-Si can yield complementary insight into the structure of a-Si on the length-scale up

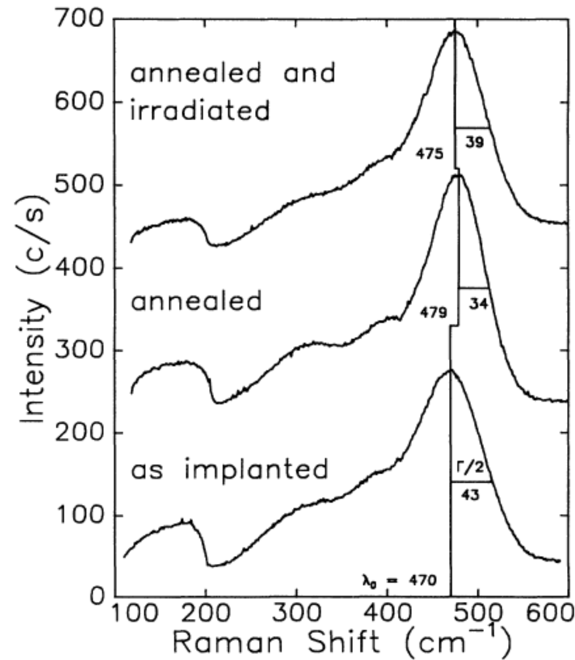

Figure 1.2: Typical Raman spectra of as-implanted, annealed implanted (500°C, 45 minutes) and re-irradiated, annealed implanted a-Si obtained by Raman microspectroscopy by Roorda *et al.* [13].

to ∼6 Å.

Intriguingly, it has been difficult to create models from first principles, i.e. *ab initio* models, of a-Si in good agreement with all experimental data, and to date no such model exists [32, 33]. As early as 1975 an attempt to model amorphous semiconductors was performed by Beeman *et al.* [34], who gradually modified original hand-built CRN models with a computer. By varying the number of odd- and even-membered rings they were able to create RDFs with a large enough bond-angle deviation to replicate the experimental RDF of a-Ge. Usually, 5-, 6- and 7-membered rings are expected for a-Si or a-Ge, whereas their crystalline counterparts only have 6-membered rings. Later Wooten *et al.* [35] were able to create *ab initio* models of a-Si using a bond-switching algorithm, the so-called Wooten-Winer-Weaire (WWW)-models. Interestingly, these WWW-models with their four-fold coordination predict a-Si to be 3%-4% more dense than c-Si [35] and indeed most models of fully four-fold coordinated CRN observe such an increased mass density. Since 1987 a-Si structures have also been generated by molecular-dynamics (MD) simulations [36, 37] with the usual approach being to quench the amorphous network from the melt. These structures tend to develop coordination defects, although over-coordination rather than under-coordination [36–39], and their mass density is usually a few percent lower than that of c-Si [37, 39]. In addition, these *ab initio* MD models can also be investigated for structural order on length-scales beyond the short-range order,

although no correlations of order were observed [38]. More recently, another method of *ab initio* modelling, the activation-relaxation technique, has been employed to simulate structural models [40, 41]. This also resulted in a-Si models with lower mass density than c-Si, but less over-coordination than MD models.

These simulated models are usually compared to structural data obtained from experiment such as RDFs [36–39, 41] or the vibrational density of states [36, 38, 39]. Indeed, a recent MD study of hydrogenated a-Si (a-Si:H) suggested that RDFs are insufficient for the validation of a model, and that vibrational spectra are in fact required [42].

A fundamentally different approach to the modelling of amorphous networks is to construct the model from known experimental facts by reverse Monte-Carlo (RMC) modelling. Thereby models are generated directly from experimental data by finding a set of coordinates that minimizes the difference between model and experiment. In addition to the experimental data usually a penalty term derived from information about the interatomic interactions is introduced in order to make properties such as the bond-length physical (for further details see Ref. [33] and references therein). However, the constraint provided by, for example, just the diffraction data, does not prove sufficient [43, 44]. One study [43] found many equally good models based on diffraction data allowing the fraction of tetrahedral bond angles to be anything between about 40% and 100%. Therefore, a further study by Biswas *et al.* [44] used an RDF obtained from a large WWW-model and introduced as an additional constraint that the mean bond-angle should be close to the perfect tetrahedral angle. The resulting model was in good agreement with the diffraction data obtained by Laaziri *et al.* [14] with a coordination number of 3.85 similar to experiment. However, it was also noted that RDFs do not provide a sufficient constraint and that three-body correlation functions are also required.

Neither Raman microspectroscopy nor any standard diffraction technique can reveal insight into this order beyond the atomic scale. While correlations at a length-scale longer than 3 nm correspond to polycrystallinity or LRO, the MRO has long remained elusive. With the advent of CCD cameras and fast computers however, this regime of order on a length-scale of 1-3 nm has become accessible by a specialist electron microscopy technique called fluctuation electron microscopy (FEM). The exciting insights into the MRO of amorphous materials gained by this technique will now be introduced.

1.1.2 Medium-Range Order

FEM measures the variance in the diffracted intensity in contrast to the average in diffracted intensity that is measured by diffraction techniques. Measuring the second moment in the scattered intensity distribution gives FEM access to pair-pair atomic correlation functions and hence, sensitivity to order beyond first neighbour distances and into the realm of MRO [45].

In 1997 Gibson and Treacy [47] first observed a diminished MRO upon annealing of deposited a-Ge using FEM. The high degree of MRO observed for the original as-deposited state is not consistent with a CRN and a granular structure of ∼2 nm size was proposed instead for this state. The annealed state however, was found to approach a CRN. In order to account for the high degree of MRO, the model of paracrystallinity was developed. Paracrystals are regions which possess positional disorder but retain some of the bonding topology of crystals. The disorder is due to strain created by atom misalignment at the boundaries between the paracrystals. RDFs from such an assembly are indistinguishable from RDFs from fully random networks. A similar high MRO was observed for deposited a-Si and thus the same paracrystalline model was proposed for this network [15, 48–51]. Indeed by using this model Voyles *et al.* were able to explain the apparent abrupt phase change from a-Si to microcrystalline Si with increasing deposition temperature observed by Vepřek *et al.* [52], as a continuous increase in paracrystalline MRO in the sample until crystallinity can be observed by more conventional means [15].

An example of a variance plot over the dark-field scattering angle as obtained by FEM is shown in Fig. 1.3. The data are taken from Cheng *et al.* [46] and show the variance and thus MRO of as-implanted, sputtered and annealed implanted a-Si. Clearly, the as-implanted and sputtered network display the same high variance, whereas the annealed network displays a significantly reduced variance.

One of the disadvantages of FEM however, lies in the fact that FEM data does not allow the direct inversion or refinement of the data due to severe computational difficulties caused by the large number of terms in the normalized variance. Thus the construction of a unique model of the amorphous structure is not possible from the data. Therefore,

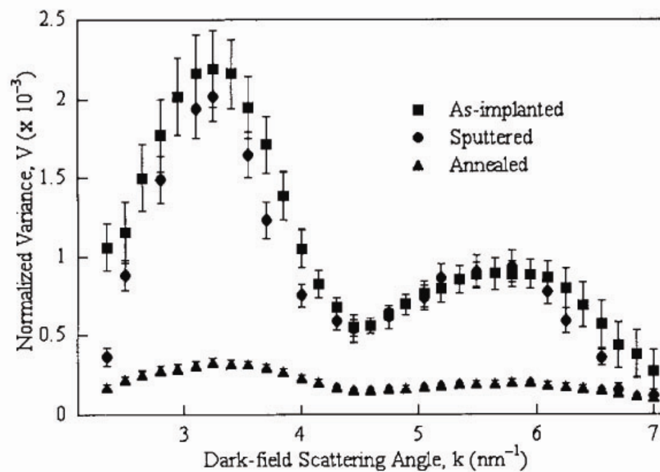

Figure 1.3: Typical variance plot for as-implanted, sputtered and relaxed implanted a-Si obtained by FEM by Cheng *et al.* [46].

these previous studies have inferred structural information from FEM data by comparing the measured variance with simulations from proposed models. While the paracrystalline model apparently fits deposited a-Ge and a-Si well [47, 48, 50, 51], another model explaining the high degree of MRO as due to voids [53, 54] fits the data equally well. This model had been obtained by a method called experimentally constrained molecular relaxation, a combination of *ab initio* and RMC modelling [53]. These very different models demonstrate the essential 'non-uniqueness' of structural models obtained by a particular solution to the FEM data. The paracrystalline model has also been used for ion-implanted a-Si [46, 55, 56], although this is somewhat controversial [57] as will be elucidated in more detail in the next section.

Nonetheless, despite the difficulty in interpreting FEM data it is clear that significant differences can be observed on this MRO-scale either due to different thermal history [15, 46, 55, 56] or preparation method [50].

The form of a-Si studied in most detail by all these techniques is ion-implanted a-Si. Moreover, the short-range ordering occurring upon thermal annealing has also been studied most thoroughly for this form of a-Si. The mechanism behind the structural relaxation will now be introduced in more detail for this example.

1.2 Structural Relaxation of Ion-Implanted Amorphous Silicon

Ion-implanted a-Si formed by self-implantation of Si ions into c-Si is the only pure form of a-Si that has been studied in detail to date. Its purity is comparable to that of c-Si and its voidless microstructure [58] makes it one of the best candidates for elucidating the nature of a model amorphous semiconductor. Additionally, its mass density approaches that of c-Si to within 2%, making it one of the most dense forms of a-Si [23]. Therefore, its structure and especially its behaviour upon thermal annealing has been investigated in much detail.

In the late 1980s it was found that upon annealing of ion-implanted a-Si a considerable decrease in the width of the Raman TO-like peak can be observed [16, 28]. An example of this has been shown in Fig. 1.2 in the previous section. Furthermore, a decrease in the intensity ratio of the TA-like to the TO-like peak was reported accompanying this decrease in peak width [28]. Both these changes in the Raman spectrum were attributed to a heat release occurring upon annealing. In 1989 Roorda *et al.* performed a series of precision differential scanning calorimetric (DSC) measurements to determine this heat release [19]. They found that a heat of approximately one-third of the heat of crystallization is released during this annealing process. This heat release is associated with the appearance of a new 'state' of a-Si, the so-called relaxed state. Moreover, the a-Si film

was fully relaxed after annealing of up to an hour at 500°C [13], indicating that this new state is independent of crystallization events as epitaxial regrowth of sufficiently thick samples is negligible under these conditions [59]. This transition from the unrelaxed, as-implanted state to the relaxed state is irreversible and is known as 'structural relaxation' or short-range ordering and is an intrinsic network rearrangement.

This structural relaxation is not unique to ion-implanted a-Si however, as Raman microspectroscopy and DSC experiments have shown that the same behaviour occurs in evaporated a-Si [13] and also electron beam evaporated a-Si [60] upon annealing. Therefore, structural relaxation is not an artifact from the preparation of a-Si by implantation. Interestingly however, a-Si quenched from a laser-induced melt was observed to be fully relaxed even before annealing [13].

The structural relaxation occurring in ion-implanted a-Si can be attributed to the annihilation of point-defects and small point-defect clusters [13]. Such defects may consist of coordination defects such as dangling bonds or of bond-defects within the network. Since atoms surrounding a defect change their position slightly to accommodate for the energetically unfavourable situation, heat will be released around a collapsing defect upon annealing. The reduction of the concentration of structural defects of 1.2 at.% in unrelaxed a-Si to 0.4 at.% in relaxed a-Si (measured by positron annihilation spectroscopy [61]) can account for this heat release. This does not contradict the notion that relaxation is short-range ordering since a decrease of defect concentration also leads to a decrease of the bond-angle distortion and thus to the observed decrease of the Raman TO-like peak width. However, the negligible change in mass density upon relaxation ($<0.1\%$) [23] puts a limit on the nature of the defect annihilation occurring during the structural relaxation. Therefore, it was concluded that the most likely explanation is mutual annihilation of low- and high-density defects such as interstitial-vacancy-recombination [13].

To gain an even more detailed insight into the structure of as-implanted and relaxed implanted a-Si a high-energy X-ray diffraction study was undertaken by Laaziri *et al.* [14]. RDFs for both states were obtained (shown in Fig. 1.1). Both states had (within 0.005 Å) the same mean bond-length as c-Si (2.35 Å) [14] indicating that the Si-Si bond is not strained. Thus the network of both states would have been expected to be more dense than c-Si as has been predicted for ideal CRNs [35]. However, a-Si was found to be slightly under-coordinated (3.79 for as-implanted a-Si and 3.88 for relaxed a-Si) [14], and this under-coordination accounts for the fact that this form of a-Si is about 1.8% less dense than c-Si [23]. The second peak of the RDF allowed a calculation of the bond-angle distortion $\Delta\theta$, which showed a decrease from 10.45° to 9.63° upon annealing [14]. This correlates well with $\Delta\theta$ obtained from Raman microspectroscopy. Furthermore, the under-coordination was attributed to the presence of vacancy-type defects which are also responsible for the density-deficit of ion-implanted a-Si [14]. Additionally, the increase in coordination number was directly correlated to a reduction in defect concentration. Due

to the negligible change in mass density observed upon annealing it was concluded that the reduction in vacancy-type defects is accompanied by a similar reduction in interstitial-type defects [14]. Such a reduction does not cause a volume change in c-Si and is therefore not expected to do so in a-Si. Indeed, subtraction of the fitted Gaussian profiles from the measured RDFs might indicate the presence of such interstitials when compared to the same procedure repeated for c-Si [14]. Therefore, this X-ray diffraction study was consistent with structural relaxation as a result of defect annihiliation, as had been inferred from previous experiments.

This reduction in defect concentration upon annealing has also been observed by MD simulations of amorphous structures [62–64]. One study [62] observed an additional narrowing of the second peak in the RDF accompanied by a decrease in the bond-angle distribution function, whereas another study found a decrease in bond-angle deviation from 15.2° to 12.5°. Indeed, a more recent study [64] identified structural relaxation as the reconstruction of dangling bonds near vacancy sites, whereby the coordination number increased from 3.94 to 3.99 and the mass density remained constant. This also provides support for the interpretation of structural relaxation as defect annihilation.

Alternatively, the as-implanted network has also been described as paracrystalline. This is inferred from the same degree of MRO observed by FEM for as-implanted and sputtered a-Si [46, 55, 56]. An example of this similar MRO of both forms of a-Si has been shown in Fig. 1.3 in the previous section. This paracrystalline MRO in ion-implanted a-Si was explained according to an 'energy spike model' of ion-implantation [65]. The MRO was largely observed to disappear upon annealing, as also seen in Fig. 1.3, and hence the removal of paracrystals was proposed as part of the mechanism behind relaxation [55]. Thus the process of relaxation was thought to have two phases [56]: Firstly, short-range ordering, i.e. collapsing of defects, is taking place at low temperature. Secondly, medium-range disordering is taking place, i.e. the paracrystals collapse into a CRN, and the short-range ordering is completed.

This model and mechanism however, are somewhat controversial [57]. For example, the FEM study only detected changes in MRO upon annealing at 500°C and higher, whereas structural relaxation (as measured by calorimetry for example) commences well below room temperature [57, 66]. Additionally, the MRO (in Refs. [46, 55, 56]) seems to continuously decrease with annealing time (up to 285 min at 500°C) rather than stabilize at the level expected of an 'anneal stable' relaxed state. Moreover, a significant difference in MRO was reported in the study by Cheng *et al.* [46, 56] between the surface and deep region [46, 56] raising the possibility that the surface of the material studied was not fully amorphized by the implant conditions used. Even if the surface appeared 'diffraction amorphous' it might have consisted of a 'pre-amorphous' highly defective state, rather than the form of a-Si referred to as 'as-implanted' a-Si in the current work. Interestingly, the deep region was identified as a highly defective CRN rather than as paracrystalline

[56], but no mention was made of the influence of thermal annealing on this deep region.

Thus, in summary, it can be said that two distinct states of ion-implanted a-Si clearly exist: the as-implanted (unrelaxed) a-Si network consisting of an imperfect CRN with a high defect concentration and the relaxed network which approaches an ideal CRN.

Intriguingly, these different states also behave substantially differently upon indentation testing as has been shown by our earlier work [21, 22]: whereas the as-implanted state was observed to deform via plastic flow, the relaxed state deforms via a *phase transformation*. Cross-sections of residual indent impressions prepared for transmission electron microscope (TEM) investigation are shown in Fig. 1.4. The figures are taken from our earlier work [21] and show a bright-field image of a residual indent in as-implanted a-Si in Fig. 1.4(a) with a selected area diffraction pattern (SADP) from beneath the residual indent as an inset. The bright-field image in Fig. 1.4(a) reveals only amorphous material and no evidence of crystallinity is observed, which is supported by the SADP. This is very different for relaxed implanted a-Si as can be seen in the dark-field image of a residual indent in Fig. 1.4(b). The SADP taken from beneath the residual impression is shown as an inset and clearly reveals spots which cannot be attributed to the normal diamond cubic

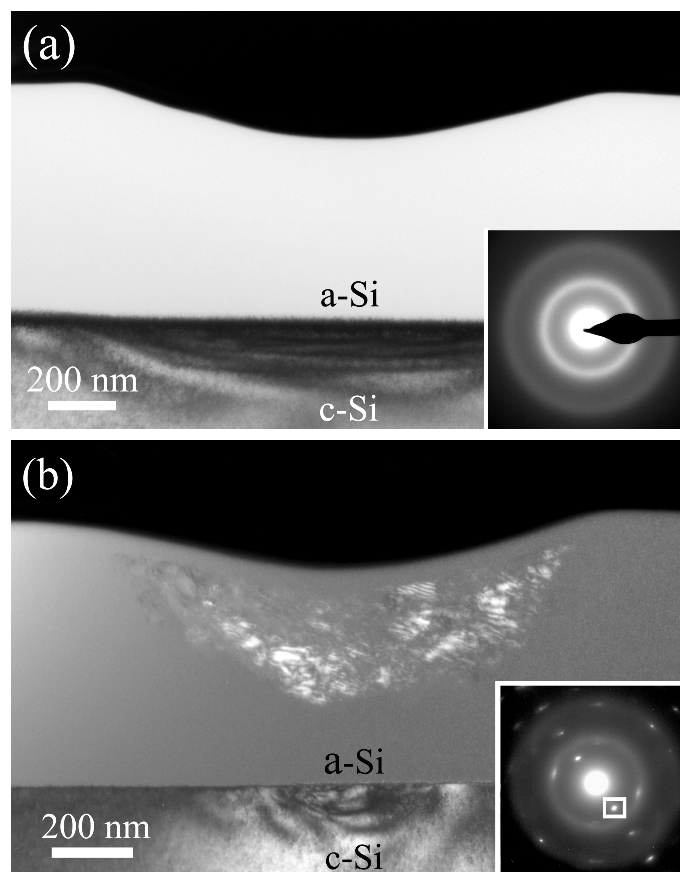

Figure 1.4: Cross-sectional TEM from residual indent impressions made in (a) as-implanted and (b) relaxed implanted a-Si as reported by Haberl *et al.* [21]. SADPs taken from beneath the residual impressions are shown as insets in both cases.

form of silicon, but to other crystalline phases of silicon with bc8 or r8 structure. The spot marked with a box[a] had been used for the dark-field image shown in Fig. 1.4(b) which reveals a considerable amount of these crystalline phases beneath the impression.

Clearly the indentation behaviour of ion-implanted a-Si, or at least the pressure-induced transformation behaviour of the relaxed state, is closely related to the phase transition behaviour of crystalline silicon under high-pressure [21, 22]. Therefore, the high-pressure behaviour of c-Si and a-Si will be introduced in the next section.

1.3 High-Pressure Behaviour of Silicon

1.3.1 Phase Transitions in Crystalline Silicon

The high-pressure behaviour of c-Si has attracted wide interest for five decades now and its phase transition behaviour has been explored up to $\sim$250 GPa. To date twelve different crystalline phases have been reported in this pressure regime. A short summary of the phase transition behaviour will be presented now. For an extensive overview refer to Ref. [67] and references therein.

The main crystalline structures forming upon loading and unloading in a diamond-anvil cell (DAC) are shown schematically in Fig. 1.5. Note that the diverse phases are not numbered according to the pressure-regime they are stable in but according to their historical discovery. Upon compression to $\sim$11 GPa silicon transforms from its diamond cubic structure (Si-I) to a metallic phase with β-Sn structure (Si-II) [68–70]. Above $\sim$13 GPa this phase is distorted to the orthorhombic $Imma$ structure (Si-XI) [71, 72]. This structure transforms completely into a simple hexagonal structure (Si-V) at 15.4 GPa [71, 72]. Above $\sim$38 GPa another orthorhombic structure (Si-VI) with $Cmca$ space group forms [73], which converts to the hexagonal close-packed structure (Si-VII) [74] at $\sim$42 GPa. Finally, at $\sim$79 GPa the face-centred cubic structure (Si-X) [74] is found, which is stable up to 248 GPa, the highest pressure probed to date. For details on these high-pressure phases of silicon, their crystal structures and space groups, refer to Appendix A, Section A.1.

Upon unloading these phase transitions are reversible until the metallic Si-II is reached as this form of silicon cannot transform back to the diamond cubic Si-I phase [67, 75, 76]. In 1962, Minomura *et al.* noted the enhanced electrical conductivity of silicon samples after pressure release from the metallic Si-II phase [68]. The remaining end phase was later identified as bc8 (Si-III), a body-centred cubic structure [77, 78]. This phase was thought to transform straight from Si-II at a pressure of $\sim$8 GPa [69, 79] and it was found to be a semimetal with a resistivity of less than 0.1 Ωcm [70, 80]. Upon thermal

[a]Note that SADPs from residual indent impressions are not usually indexed in the traditional manner due to the very small crystal size and their instability. For further details refer to Appendix A, Section A.2.

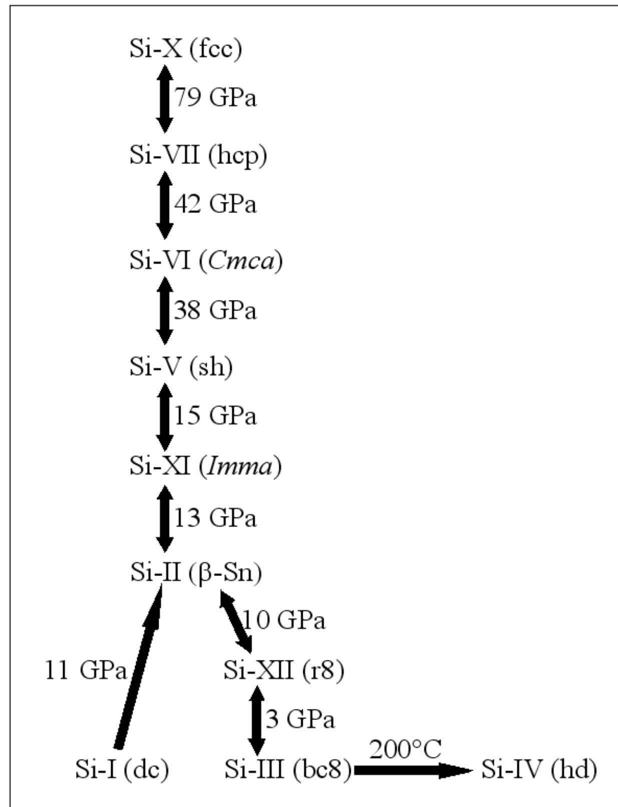

Figure 1.5: Schematic representation of the phase transitions observed for c-Si under DAC loading and unloading.

annealing at 200°C it was reported to transform to the hexagonal diamond structure (Si-IV) [70, 80]. However in 1994, Crain *et al.* observed that Si-II does not transform directly to Si-III, but rather to a distorted form of Si-III first [81]. This was identified as r8 (Si-XII), a phase with rhombohedral structure [81, 82]. Si-XII starts to nucleate from Si-II at $\sim$10 GPa until all Si-II is transformed at 6.2 GPa. Below 3.2 GPa a mixture of Si-III and Si-XII is found and at ambient pressure only a small amount of Si-XII is left. By re-compression up to 2.5 GPa Si-III is nearly completely transformed back to Si-XII indicating a reversible transformation [81]. The electronic band structure of silicon in the r8 structure was calculated to be semimetallic [82]. Later this transformation pathway of Si-II to Si-XII and then Si-III was confirmed by *ab initio* calculations [83]. However, Si-XII is more likely to be a narrow bandgap semiconductor than a semimetal [83]. The details of these crystalline phases of silicon that appear upon unloading are also given in Appendix A, Section A.1.

The situation is different when porous Si, which contains nanometre-sized domains of diamond-structured material, is pressurized in a DAC [84]. Pressure-induced amorphization of c-Si was observed in this case, whereby this high-density a-Si resembles structurally the β-Sn crystalline form with coordination greater than 4. Upon decompression from $\sim$10 GPa a low-density form of a-Si started to appear, which was the only form

of silicon left after complete decompression. Another study also observed the formation of a-Si from Si-II after decompression [85]. However, this remaining a-Si was only formed when heating a quenched Si-II phase from 100 K to 300 K at a constant pressure of 1.5 GPa. Indeed this latter study indicates that the transformation from Si-II to a-Si in a DAC seems to be temperature dependent, consistent with studies by Brazhkin *et al.* who clearly observed the formation of a-Si solely at temperatures below 120 K [86, 87].

Summarizing the DAC behaviour of silicon it can be said that bulk Si-I transforms always to Si-II and further high-pressure phases upon loading whereas, upon unloading at room temperature, Si-II transforms always to other crystalline phases regardless of the rate of the unloading.

The high-pressure behaviour of c-Si has also been studied using indentation. An early indentation hardness study of c-Si indicated already that a semiconductor-metal transition occurs and that this behaviour determines the measured hardness value [88]. Electrical measurements established that c-Si undergoes a phase transformation to a metallic phase during loading [89–91]. Using spherical indentation the mean pressure at the onset of the transformation during loading was calculated to be 11.3 GPa and of the reverse transformation during unloading to be 8.4 GPa [92, 93]. These pressures agree well with the pressure values found in DAC experiments for the transformation from Si-I to Si-II and from Si-II to Si-III/Si-XII. However, it is only after 'slow' unloading that Si-III and Si-XII form in residual indents, while a-Si was found after 'fast' unloading even at room temperature. This behaviour has been confirmed by Raman microspectroscopy [94–97] as well as cross-sectional TEM (XTEM) [97–100].

Examples of Raman spectra of such residual indents made in c-Si after fast and slow unloading are shown in Fig. 1.6. The high-pressure phases resulting from the slow unloading are labelled according to Ref. [101]. Further details of the Raman bands are given in Appendix A, Section A.2.

A dark-field TEM image of a cross-section of a spherical indent impression in c-Si after intermediate unloading is shown in Fig. 1.7. The SADP taken from beneath the impression is shown as an inset and the spot from the high-pressure phase used for the dark-field imaging is marked with a box. A thin layer of a-Si (marked with arrow 1) is visible on the top surface which was caused by the focused-ion-beam system during sample preparation [102]. Intermediate unloading in this context means that the unloading was performed slow enough to nucleate some crystalline high-pressure phases (marked with arrow 2), but fast enough to also form some a-Si (marked with arrow 3). Beneath the phase transformed zone slip planes (marked by arrow 4) are seen, a typical feature of residual impressions made in c-Si.

Interestingly, upon annealing of the high-pressure phases nucleated by indentation, Si-IV is formed but there is also strong evidence of a new, crystalline phase, the so-called Si-XIII, as observed by Raman microspectroscopy [103]. The structure of this phase is

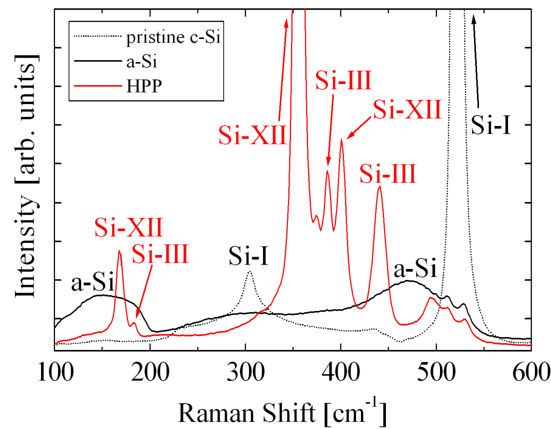

Figure 1.6: Raman spectra of residual indent impressions in c-Si after fast and slow unloading resulting in the formation of a-Si and the crystalline high-pressure phases, respectively. The indentations were performed using a spherical ∼18 µm tip applying a maximum load of 750 mN.

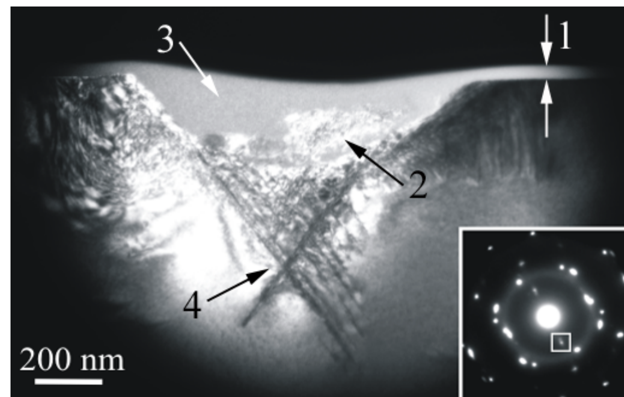

Figure 1.7: Dark-field image of a cross-sectional TEM specimen of a residual indent impression in c-Si. An SADP taken from beneath the residual impression is shown as an inset. The indentation was performed using a spherical ∼2 µm tip applying a maximum load of 20 mN.

still unresolved although it possibly has a large unit cell with hexagonal symmetry. Details of this new phase of Si are also given in Appendix A, Section A.3.

The phase transformation behaviour of c-Si is clearly different in indentation and DAC experiments: Si-II can transform to a-Si at room temperature upon indentation unloading and a new crystalline phase, Si-XIII, may be formed upon annealing. These differences are most likely due to the very different stress states, since shear stresses play a significant role in indentation testing whereas DACs experiments are 'purely' hydrostatic. Additionally, considerable residual stresses remain after indentation unloading as a result of the highly non-uniform stress during loading in contrast to DAC testing, where the pressure is more uniform and appears to be fully released on decompression.

1.3.2 Phase Transitions in Amorphous Silicon

Clearly, the relaxed state of implanted a-Si phase transforms under indentation testing as seen from Fig. 1.4 [21, 22]. Therefore, the question arises as to which transformation pathway it follows and how that ties in with previous high-pressure DAC experiments on a-Si and/or c-Si. Although many properties of a-Si have been extensively studied, not much is known about its high-pressure and deformation behaviour. Nonetheless, a number of key publications [21, 85, 89, 104–106] exist and will be summarized now.

In 1974 Shimomura *et al.* [104] found that vacuum-evaporated a-Si transformed upon loading in a diamond-anvil cell to a metallic phase that was consistent with a high-density phase of a-Si (HDA). After unloading however, this HDA had transformed back to low-density a-Si (LDA). Interestingly, the onset of the transformation of a-Si to its metallic phase occurs at lower pressure than is observed for c-Si ($\sim$66% of the pressure necessary for c-Si). A further study also proposed that a-Si should undergo a transformation to a high-density (metallic) amorphous phase during loading and transform back to its original LDA state during unloading [105]. Additionally this study reported the co-existence of the HDA and LDA phases in a pressure regime from 8 GPa to 4 GPa upon unloading. The a-Si used for this study was prepared by a ‘solid-state chemical metathesis synthesis route’ resulting in a hydrogen content of $\sim$7 at.% [107]. Also, a more recent extended X-ray diffraction study of the high-pressure behaviour of the same form of a-Si reported the formation of HDA as well as Si-II upon loading [106]. In this study however, more HDA than Si-II was always observed and so it focused on the properties and characteristics of this metallic HDA phase. Moreover, upon unloading only LDA silicon remained.

Only one report of DAC experiments on a-Si (prepared by glow-discharge decomposition of silane) provides some evidence for a transformation to Si-III on pressure release [85]. This study found that a-Si transforms into Si-II at a pressure of 10 GPa and after pressure-release from this maximum pressure solely a-Si was recovered. However, upon decompression from a higher maximum pressure of 12.8 GPa, Si-III was formed. Note that Si-XII was unknown at the time of this study. It is unclear why this last study (that observes a crystalline Si-III end phase) differs from all other DAC studies of a-Si (where the end phase is always LDA silicon).

To date little indentation work has been done to investigate the phase transition behaviour of a-Si. One indentation experiment on a-Si (prepared by homogeneous chemical vapour deposition) indicated a (reversible) transformation to an electrically conducting phase under loading [89]. The remaining phase after unloading was LDA. However, it was concluded that the rapid unloading rates used (unloading within 30 ms) might cause this phase transformation to a-Si. Another indentation study on sputtered a-Si reported no evidence of phase transformation even after many cycles of loading [108], although a further study on various sputtered films observed random nucleation of the high-pressure

phases in some instances [109].

In conclusion, the high-pressure behaviour of a-Si seems significantly different to the high-pressure behaviour of c-Si in DAC as well as indentation experiments. Whereas c-Si in room temperature DAC experiments will always nucleate the crystalline high-pressure-phases upon unloading, a-Si is more likely to transform back to its LDA form. However, no DAC studies have been performed on pure a-Si, only on forms containing a significant amount of impurities such as hydrogen, a fact which might account for some of the observed discrepancies. Similarly, indentation experiments on forms of a-Si other than relaxed implanted a-Si are most likely to observe the formation of a-Si after indentation unloading. Therefore, the indentation behaviour of relaxed implanted a-Si seems to be more similar to the indentation behaviour of c-Si and is inconsistent with the DAC studies on a-Si. Thus, in this study the phase transformation behaviour of pure a-Si will be compared to its crystalline counterpart rather than previous high-pressure work on a-Si.

1.4 Thesis Structure

An outline for the structure of this thesis follows. Note that the implications of the results for the broader understanding of a-Si will not be discussed in depth at the end of each respective chapter. Instead all the significant results will be collated and discussed in the form of a framework for the overall understanding of the structure of a-Si in a concluding chapter (Chapter 8).

- In Chapter 2 the various experimental techniques used will be described. First indentation and its two major uses, hardness measurements and nucleation of a phase transformation, will be detailed. Thereafter some information will be given on Raman microspectroscopy with focus on the analysis of a Raman spectrum of a-Si. Lastly, some background details to the various transmission electron microscopy techniques, namely electron diffraction, fluctuation electron microscopy and electron-energy-loss spectroscopy, will be given.

- In Chapter 3 some background on the various forms of a-Si used in this study will be presented, namely a-Si made by plasma-enhanced chemical vapour deposition, magnetron-sputtering, quenching from a laser-induced melt, ion-implantation and a structural collapse from the dense metallic Si-II phase induced by fast indentation unloading. After the background information on each form, the experimental conditions for the formation will be summarized.

- In Chapter 4 results from preliminary investigations of the various film properties will be detailed. These basic investigations concern such properties as uniformity of the film, crystallinity, impurity content and mass density. Based on the outcome of these investigations the methods used to study the individual a-Si films are chosen.

- In Chapter 5 the mechanical properties, i.e. deformation behaviour and indentation hardness, of the various films will be described. All films were studied for their deformation behaviour, e.g. phase transformation or plastic flow, to obtain a first 'measure' of structural differences between the various films. However, only the uniform films were probed for their indentation hardness as only these forms allowed meaningful analysis of this property.
- In Chapter 6 the results of the investigation of the structural properties of the uniform films on the MRO-scale as studied by fluctuation electron microscopy will be presented.
- In Chapter 7 the results obtained for the atomic scale order will be elucidated. Only the pure forms of a-Si were studied for their nearest-neighbour characteristics by electron diffraction, as interpretation of RDFs from impure films is not straightforward. Moreover, all uniform films were studied by Raman microspectroscopy for their vibrational properties.
- In Chapter 8 the key results will be discussed in detail. The information on the structural properties gained from the variety of techniques used and from the various films will be used to create an extensive framework for the understanding of a-Si. In addition, concluding remarks will be given.
- In Chapter 9 some proposed future experiments and simulations will be outlined.
- Finally, several appendices are included which contain more detailed information on methods, analyses and results that are related to, but somewhat tangential, to this thesis.

Chapter 2

Characterization Techniques

A multitude of experimental techniques was used to investigate the structure of the various forms of a-Si. The background to each of these techniques will be presented in this chapter.

Nanoindentation was used to determine the deformation behaviour and possible phase transformation behaviour as this behaviour may give insight into the 'state' of the amorphous network [22]. Additionally, it was also used to investigate the indentation hardness as changes in hardness might reveal more subtle changes in the structure of the amorphous network.

Raman microspectroscopy was used to study the vibrational properties of the various forms of a-Si as these are very sensitive to changes in the amorphous network and especially the structural relaxation.

A variety of transmission electron microscopy (TEM) techniques was employed. Conventional TEM was used for a preliminary study of all the amorphous films, but also to study residual indent impressions and to search for further evidence of phase transformations. Quantitative electron diffraction was used to obtain the radial distribution function of the pure forms of a-Si (ion-implanted and PI) in order to gain insight into the structural properties at the atomic scale. Fluctuation electron microscopy (FEM) was conducted on the uniform films of a-Si (sputtered, ion-implanted and PI) to study the structural properties beyond the length-scale accessible by diffraction. And lastly, electron-energy-loss spectroscopy (EELS) was used to investigate the mass density of the pure forms of a-Si.

2.1 Nanoindentation

Indentation was initially conceived as a method to measure the hardness of materials, usually by using a hard steel ball as an indenter. Nowadays indenters, either pyramidal or spherical, are mostly made from diamond. Indentation is a very simple technique, where the sharp indenter tip is forced down into the material whereafter the applied force and the area of the residual impression are used to determine the mechanical properties hardness, H, and elastic modulus, E. Unlike the elastic modulus or Poisson's ratio however, hardness is not a fundamental material property. Perhaps the best definition of it is as 'the resistance of a material to deformation by another material' [110]. Hence the indentation hardness (or Meyer's hardness) H can be defined as:

$$H = \frac{P_{max}}{A} \tag{2.1}$$

in which P_{max} is the maximum applied load and A is the projected area of the residual impression [110].

In order to calculate the hardness traditional indentation techniques need to image the residual indent impression. This was originally done by optical imaging, but is not as

easily accomplished for micron-sized indent impressions. Indentation can be performed throughout the elastic and plastic regimes. Indentations in the elastic regime do not leave any residual impressions on the surface as opposed to the plastic regime where the sample will have undergone permanent deformation.

The first to analyse this in depth was Hertz [111] when he considered the elastic contact problem - the elastic contact between two spherical surfaces with different radii and elastic constants. Further general relationships between load, displacement and contact area for any punch tip which can be described as a solid of revolution of a smooth function were derived by Sneddon [112]. He showed that the load-displacement relationships for many simple punch geometries can be written as:

$$P = \alpha h^m \tag{2.2}$$

where P is the indentation load, h the elastic displacement of the indenter and α and m power law fitting constants.

2.1.1 Oliver-Pharr Method

To overcome the limits of optical imaging of residual impressions for the determination of hardness and elastic modulus, Oliver and Pharr introduced the instrumented indentation technique in 1992 [113]. Instrumented indentation, or nanoindentation, accomplishes this by continuously measuring the applied load and indentation depth throughout the whole test duration. Originally this technique was developed for sharp indenters, like a Berkovich indenter tip. A Berkovich indenter is a three-sided pyramidal tip with a total included angle (angle from one edge to the opposite side) of 142.3 degrees. The half-angle, or the angle from the perpendicular to one face, is 65.3 degrees.

A schematic representation of a typical load-displacement curve obtained during indentation with a Berkovich indenter is shown in Fig. 2.1. Here P denotes the applied load and h the displacement relative to the pristine surface. The deformation is assumed elastic and plastic whereby only the elastic component is recovered upon unloading. It is this elastic nature of the unloading curve that facilitates the analysis.

Three parameters are measured during an indentation test, the maximum load P_{max}, the maximum displacement h_{max} and the contact stiffness of the upper part of the unloading curve $S = dP/dh$. Since load-displacement curves obtained from indentation tips with non-punch geometry are curved, the power law shown in Eq. 2.2 has to be modified (with h_f being the final depth) to:

$$P = \alpha (h - h_f)^m \tag{2.3}$$

The best approximation for Berkovich indenters is a description as a paraboloid of revo-

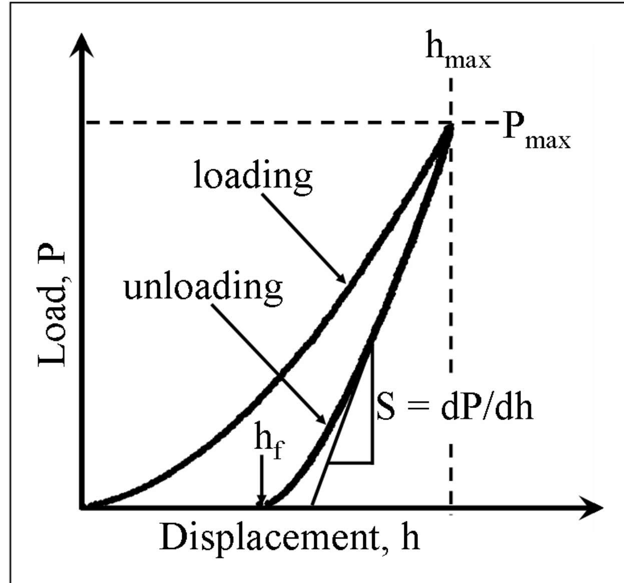

Figure 2.1: Schematic illustration of load-displacement data obtained from an indentation experiment according to Oliver and Pharr [114].

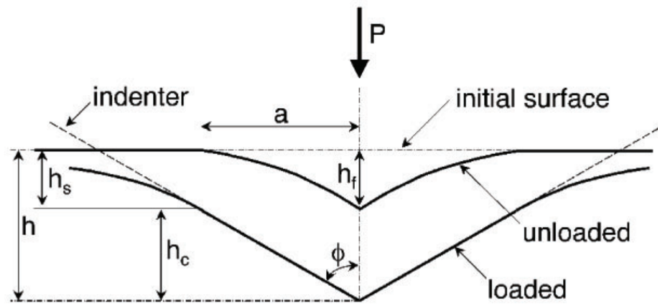

Figure 2.2: Schematic illustration of the unloading process showing the parameters characterizing the contact geometry. This schematic was taken from Oliver and Pharr [114].

lution with $m = 1.5$.

The procedure used to measure H and E is based on the unloading processes shown schematically in Fig. 2.2. The basic assumption therein is that the contact periphery 'sinks in' in a manner that can be described by indentation of a flat elastic halfspace with rigid punches of simple geometry. This does not account for 'pile-up', which is material that flows out from under the tip during indentation loading. Assuming however, that pile-up is negligible, the elastic models show that the amount of sink-in, h_s, is given by:

$$h_s = \epsilon \frac{P_{max}}{S} \tag{2.4}$$

Therein ϵ is a constant which depends on the geometry of the indenter (for example 0.75 for a paraboloid of revolution). Now the contact depth $h_c = h_{max} - h_s$ can be calculated:

$$h_c = h_{max} - \epsilon \frac{P_{max}}{S} \tag{2.5}$$

Assuming a tip area function $F(d)$ that describes the cross-sectional area of the indenter at a distance d from its tip, the projected area at the contact depth h_c, in short the contact area, A can be calculated by:

$$A = F(h_c) \tag{2.6}$$

This tip area function must be carefully calibrated for each tip used in addition to the frame compliance of the indentation system. This is usually accomplished by calibration measurements of a material with known properties such as, for example, fused quartz. Once the exact contact area is determined, the hardness H can be calculated by Eq. 2.1. Similarly, the reduced modulus E^* can be calculated through its relationship to the stiffness S and contact area A by:

$$S = \frac{dP}{dH} = \beta \frac{2}{\sqrt{\pi}} E^* \sqrt{A} \tag{2.7}$$

Thereby, β is a constant best estimated as 1.05 for a Berkovich indenter tip [114]. The elastic modulus E can be determined from E^* by:

$$\frac{1}{E^*} = \frac{(1-\nu_m^2)}{E_m} + \frac{(1-\nu_i^2)}{E_i} \tag{2.8}$$

in which ν_m and E_m are Poisson's ratio and the elastic modulus of the indented material and ν_i and E_i of the indenter material (1141 GPa and 0.07 for diamond [114]).

This method has been used and verified extensively for numerous materials, but some problems remain. While the origin of the constants mentioned above has been explained by the 'effective indenter shape' theory, the problem of the 'pile-up' persists. For further details see Ref. [114] and references therein.

For brittle materials such as semiconductors often spherical nanoindentation is used for determination of the mechanical properties. The advantage of spherical indenters lies in their more uniform stress field which minimizes the cracking that occurs in these brittle materials. Field and Swain [115] developed a method in which a partial load-unload cycle is used to determine the elastic component during the indentation process. This means after each loading step, fast unloading is performed to 50% of the applied load, i.e. some of the elastic deformation is recovered. The next loading step will be to a higher load than the previous one, but again unloading to 50% of the applied load will be performed afterwards. This continuous loading and partial unloading yields data of the elastic recovery for the entire displacement regime the indentation takes place in. From this data the mechanical properties H and E can then be calculated. For further details see [115].

In this present study however, hardness is mainly measured using a Berkovich tip as cracking was not found to be an issue and some of the samples required very precise positioning of the indentation tip. This was only possible by scanning across the surface with a sharp tip in the Hysitron TriboIndenter in a similar manner to scanning in contact mode in an atomic force microscope (AFM). After the load-displacement curves were obtained from the required position, the Oliver-Pharr method [113] was used to calculate H. Additionally, some of the samples were investigated for their indentation hardness by directly imaging the residual impressions with a scanning electron microscope (SEM). This was necessary, as not only is 'pile-up' known to occur in silicon, but also the comparison of phase-transforming and non-phase-transforming materials is non-trivial. After the SEM imaging, the projected area as defined by the apexes of the triangle (i.e. of the resulting Berkovich nanoindent) was measured using the package ImageJ [116] and then H was directly calculated using equation 2.1.

2.1.2 Evidence of Phase Transformation Directly from Load-Displacement Curves

Indentation is not only a useful technique for probing mechanical properties, but also for nucleating pressure-induced phase transformations. Interestingly, these phase transformations are not only evident upon investigation of residual impressions by Raman microspectroscopy or cross-sectional TEM, but are also represented in the load-displacement curves.

For indentation of c-Si a discontinuity, the so-called 'pop-out' event, can be observed upon unloading. This event is attributed to the phase transformation from Si-II to the crystalline high-pressure phases Si-III and Si-XII [96, 117, 118]. This phase transformation occurs via a sudden nucleation of the high-pressure phases rather than a gradual transition and is associated with a greater than 10% increase in volume. Thus, the sudden expansion of the phase transformed volume under the indentation tip will push the tip out of the material thus reducing the indentation depth. This is the 'pop-out' event observed. By using spherical indentation a second discontinuity, the so-called 'pop-in' event, can be observed during loading [93, 98, 119]. This 'pop-in' event occurs when the material that had transformed to Si-II flows out from under the indenter [98, 119]. These events upon loading and unloading are shown in an example obtained from c-Si in Fig. 2.3(a).

Upon fast unloading a more gradual change in slope, a so-called 'elbow' event is observed. For pyramidal indenters, this indicates the formation of a-Si at unloading [96, 118, 120]. However, when using spherical indenters an 'elbow' event does not necessarily mean that solely a-Si has been formed in the residual indent, the nucleation of some volume of the Si-III/Si-XII phases is also possible [121]. Thus, while a 'pop-out' event means that the high-pressure phases have been formed, an 'elbow' event indicates only

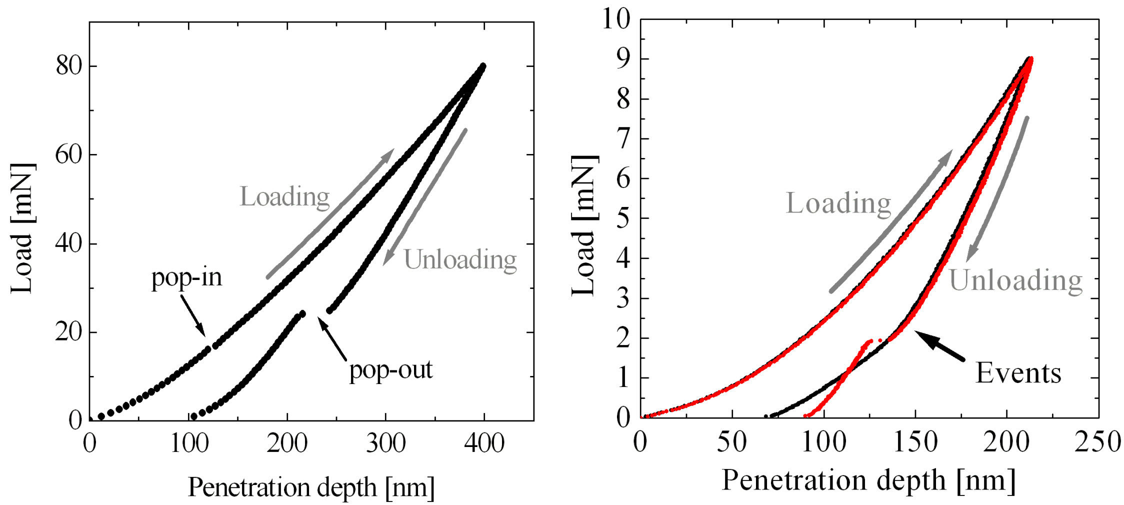

Figure 2.3: (a) Load-displacement curve of a spherical indentation performed on c-Si in the UMIS. The spherical tip used had a radius of ∼5 µm. (b) Load-displacement curves of Berkovich indentations performed on c-Si in the Hysitron TriboIndenter. The events are marked with an arrow. In both parts of the figure the loading- and unloading is indicated.

that Si-II had been formed during loading, which transforms to either a-Si and/or the high-pressure phases during unloading. Nonetheless, when using a Berkovich tip as in the Hysitron TriboIndenter an 'elbow' event usually indicates the formation of a-Si and a 'pop-out' event the formation of the crystalline high-pressure phases. Examples of these two events possible upon unloading are shown in Fig. 2.3(b). The 'elbow' event is marked with an arrow. In contrast to the load-displacement curve obtained from the spherical indentation an event like the 'elbow' event can also be observed for the curve exhibiting a 'pop-out' event. This may indicate that prior to the nucleation of the high-pressure phases some a-Si formed under the indentation tip.

Regardless of whether an 'elbow' or a 'pop-out' event, i.e. phase transformation to the high-pressure phases or to a-Si, is observed upon unloading, both events clearly confirm that Si-II had been formed under the indentation tip. Therefore, only the complete absence of any event suggests deformation via plastic flow or compression rather than phase transformation. Thus, the investigation of load-displacement curves is a very useful method when searching for evidence of phase transformation. It is also noteworthy that this phase transition behaviour makes it very difficult to assess any potential heat arising from the work by the indentation. Since the majority of this work is transformed into phase transition however, any heating effects are expected to be very small.

This phase transformation behaviour has also proven very useful for the investigation of the 'state' of ion-implanted a-Si as reported previously [21, 22]. As shown in Fig. 2.4 only the load-displacement curve obtained from relaxed implanted a-Si exhibited any events indicating that it deformed via a phase transformation, whereas the as-implanted a-

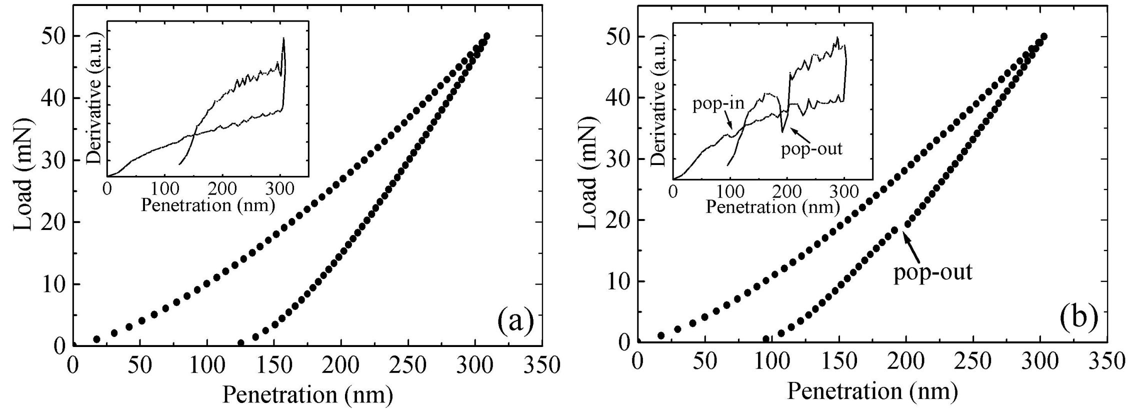

Figure 2.4: Load-displacement curves of indentations performed on (a) as-implanted and (b) relaxed implanted a-Si. The derivative of the curves are shown as insets in both cases and any occurring events are marked with arrows. These figures are taken from Haberl *et al.* [22].

Si deformed via plastic flow. This different behaviour is clearly indicative of the different 'states' of as-implanted and relaxed implanted a-Si [21, 22].

2.1.3 Experimental Details

Two different indentation systems were used in this study, an ultra-micro-indentation-system (UMIS) 2000 and a Hysitron TriboIndenter. The UMIS was used for large scale indentations and when relatively high loads were required and the Hysitron TriboIndenter was used when precise positioning of the indentation tip or thin films were investigated.

In the case of the UMIS, load is applied to the tip via a system of leaf springs by expansion of a piezoelectric device. When the indenter makes contact with the sample, the springs deflect. This deflection is measured by a force linear variable differential transformer (LVDT). The feedback system can control the load by means of this force LVDT, which is attached to the main carriage and provides the piezo with a signal. The displacement of the shaft relative to the frame of the instrument is measured separately by a depth LVDT which is attached to this frame. During indentation the load is increased in specific steps (or increments). A 'continuous load-unload cycle' is the standard test on the UMIS. Thereby, the indenter is loaded to the maximum load (and therefore maximum penetration depth) and then withdrawn. The load and unload sections can be split up into a set number of increments, whereby the force and load are measured at each step. An example of such a cycle is shown in Fig. 2.5.

The Hysitron TriboIndenter used throughout this study possesses an optical microscope in line with a nanoindenter and an AFM. The nanoindenter combines a piezo scanner similar to those used for conventional atomic force microscopy with a three-plated capacitive transducer which is used as both the actuator and sensor of the instrument. By

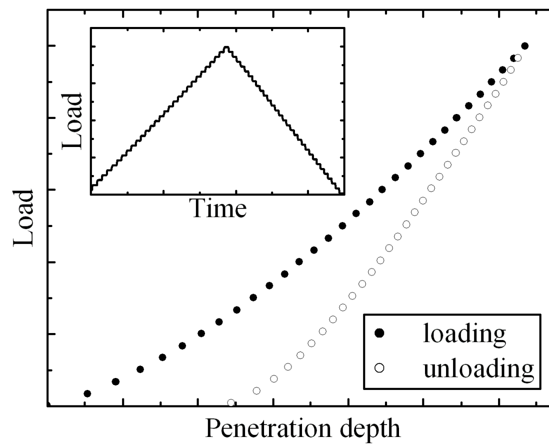

Figure 2.5: Schematic of the continuous load-unload cycle applied in the UMIS. A load versus time plot is shown as an inset displaying how the UMIS holds each step for a certain time to control the applied load.

using an XYZ-stage the diamond tip used for testing is placed close to the desired surface feature. Thereafter, the piezo scanner is used to approach the sample surface. The piezo scanner also enables *in situ* imaging, which is scanning probe microscopy (SPM) of the sample surface with the same tip as used for indentation testing. By applying a DC voltage to the bottom plate of the transducer a force is applied to the indenter tip which is fixed to the middle plate. Since the electric field potential between the plates varies linearly with the displacement of the tip and the middle plate it is attached to, the displacement of the tip can be measured accurately. As opposed to the 'continuous load-unload cycle' of the UMIS an 'open loop' cycle was used for the Hysitron TriboIndenter. Thereby, the load is applied continuously rather than stopping after each increment in order to accurately settle the tip at a given load. Due to the superior drift-correction of the Hysitron, the accurate load and penetration depth could nonetheless be determined after the indentation took place.

Throughout the entire study two different types of diamond tips were used. For indentation with the UMIS two different spherical tips with radii of ~5 µm and ~18 µm were used. The large tip was used to create large residual impressions, which were in turn further investigated using the Hysitron TriboIndenter. In this case, the applied maximum load was between 700 and 750 mN resulting in a maximum penetration depth of ~1000 nm and these indents will be referred to as 'microindents' throughout this study. The smaller spherical tip was used to investigate the deformation behaviour of various a-Si films. In this case a maximum load of 80 mN was applied resulting in a maximum penetration depth of ~400 nm. In the case of the Hysitron TriboIndenter pyramidal Berkovich tips were used. The maximum load ranged from 5 to 10 mN resulting in maximum penetra-

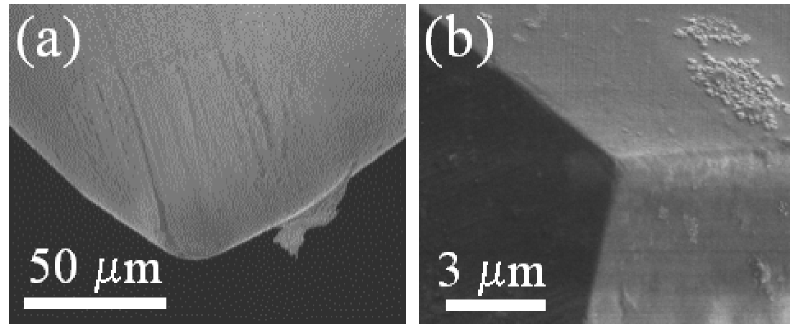

Figure 2.6: SEM scans of (a) the ∼18 μm spherical and (b) the Berkovich diamond indentation tips.

tion depths up to ∼200 nm. These indents made with the Hysitron TriboIndenter will be referred to as 'nanoindents' throughout the present study. SEM images of the large spherical and a Berkovich tip are shown in Fig. 2.6.

2.2 Raman Microspectroscopy

Raman scattering is the inelastic scattering of a photon by the electrons of molecules or crystal atoms. It corresponds to the absorption and subsequent emission of a photon via a virtual vibrational energy state. There are three possibilities for such an event, namely no difference between incident and scattered frequency, a shift to a lower frequency or a shift to a higher frequency. In the first case no energy exchange takes place meaning the light scattered elastically via so-called Rayleigh scattering. In the second and third cases, the Raman effect is observed, i.e. an energy transfer occurs. A shift to a lower frequency of emitted light, the so-called Stokes scattering, is observed when the molecule absorbs energy, while a shift to a higher energy, the so-called anti-Stokes scattering, is observed when the molecule loses vibrational energy. The energy of the scattered photons ΔE_s is thus the energy difference between the energy of the incident photons $\Delta E_i = h\nu_0$ and the vibrational states $\Delta E_\nu = h\nu_\nu$:

$$\Delta E_s = h(\nu_0 \mp \nu_\nu) \tag{2.9}$$

with the minus-sign indicating the Stokes-scattering and the plus-sign indicating the anti-Stokes-scattering. For further details refer, for example, to Refs. [122] or [123].

In crystals, only specific phonons are allowed to undergo a Raman transition or are 'Raman active'. This is determined by the polarizability tensor α as only in the presence of a non-zero derivative of the polarizability with respect to the vibrational mode Q a Raman transition or shift can be activated optically. While thus in crystals the Raman scattering is limited to the Raman active modes, this is different for amorphous materials

or nanocrystals. In the case of amorphous materials however, phonons are not defined due to the lack of periodic structure resulting in broad bands rather than discrete spectral lines (see, for example, Ref. [124] and references therein).

Raman (micro-)spectroscopy utilizes this effect in order to obtain a variety of information about a crystal (or molecule) such as structure (space group), crystal orientation, residual stress or even temperature. This is usually achieved by illuminating the sample with a laser and then collecting the scattered light with a CCD detector. The huge advantage of Raman microspectroscopy lies in the fact that it does not require any sample preparation as required, for example, for TEM and can still be used to investigate small volumes (< 1 μm).

Therefore, it is commonly used for the investigation of residual indent impressions, especially in silicon [94, 97, 121, 125–127]. Examples of residual indent impressions in c-Si after fast and slow unloading have been shown in Fig. 1.6 in Chapter 1. However, studies have not been limited to the phase transformation behaviour of c-Si [94, 97, 121, 128, 129] and ion-implanted a-Si [22, 130]. The development of residual stresses surrounding the indent impressions has attracted wide interest for the case of silicon and other semiconductors [95, 125, 127, 131–133]. Moreover, the formation of a new phase of silicon, Si-XIII, was first detected by Raman microspectroscopy [103]. The Raman shifts observed for the various (meta-)stable phases of silicon observed at ambient are summarized in Appendix A, Section A.2.

2.2.1 Amorphous Materials

Raman microspectroscopy is not only sensitive to different crystalline structures however, it is also very sensitive to the short-range order in amorphous materials. As the phonon-confinement yielding the discrete Raman bands observed for crystalline matter

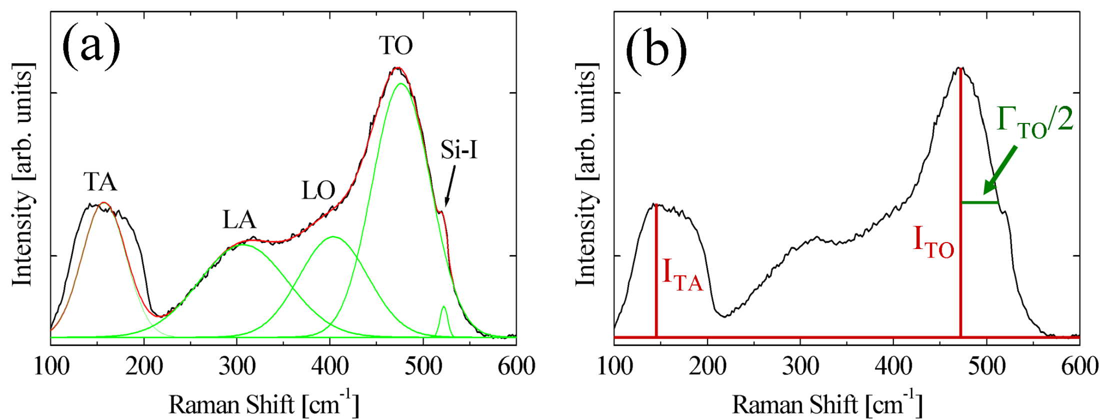

Figure 2.7: Schematic representation of (a) the peaks observed in an amorphous spectrum and (b) the characteristics used for further analysis.

does not apply to amorphous materials, inelastic scattering on all the phonon-modes can be observed. A schematic representation of a typical Raman spectrum of a-Si is shown in Fig. 2.7 with the transverse acoustic (TA)-like, longitudinal acoustic (LA)-like, longitudinal optic (LO)-like and transverse optic (TO)-like features labelled. These features are fitted by four Gaussians, although the TA-like peak is clearly non-Gaussian in profile. In addition to the amorphous profile, a small crystalline contribution can be seen from the substrate although this peak is easily accommodated by adding another Gaussian to the fitting procedure[a]. More importantly however, by only using the four 'amorphous' Gaussians for a fit, an envelope of the amorphous profile can be created thus eliminating the crystalline contribution if small. This is essential for the analysis of the spectra of some of the forms of a-Si where the laser penetrated through the amorphous layer into the crystalline substrate.

Many important characteristics of an amorphous network can be obtained from Raman spectra such as the bond-angle distortion $\Delta\theta$ or an insight into the dihedral angle deviation. The main features used for the analysis of a Raman spectrum are marked schematically in Fig 2.7(b), namely the half width at half maximum, $\Gamma_{TO}/2$, the intensity of the TO-like peak, I_{TO}, and the intensity of the TA-like peak, I_{TA}.

The characteristics of the TO-like peak are correlated to the vibrational bond-stretching modes and thus $\Gamma_{TO}/2$ can indicate whether the state of a-Si is relaxed or unrelaxed [13, 28, 30]. As mentioned in the introduction, a simple empirical equation directly relating Γ_{TO} to the mean bond-angle distortion $\Delta\theta$ has been derived by Beeman *et al.* [29]:

$$\Gamma_{TO} = 15 + 6\Delta\theta \tag{2.10}$$

However, usually $\Gamma_{TO}/2$ is used for this analysis rather than Γ_{TO} as only the high-frequency side of the TO-like peak is fully optic, whereas the lower-frequency side of the TO-like peak is overlapping with acoustic modes [30]. In the case of a purely amorphous spectrum $\Gamma_{TO}/2$ is directly determined from the maximum of the TO-like peak and the minimum on the high-frequency side. For samples with a crystalline contribution the envelope of the amorphous spectrum is first created by a fit with four Gaussians. Thereafter $\Gamma_{TO}/2$ is determined from this envelope as in the pure amorphous cases.

A further interesting quantity is the position of the TO-like peak, ω_{TO}. It has been shown that ω_{TO} will increase with increasing order [134]. When analysing this property however, it can be difficult to distinguish between influences of increasing order or increasing residual stresses as both will cause a shift towards higher wave-numbers [125]. Therefore, care has to be taken when using this property to evaluate the order present within an amorphous network.

[a] Note that the shape of a full c-Si TO peak is Lorentzian in nature. However, the fitting was performed in order to show that the c-Si TO peak is solely additive to the envelope of the Gaussian fits to the a-Si spectrum and it is therefore inconsequential whether a Gaussian or Lorentzian is used.

Information about the dihedral angle deviation can be accessed by means of the intensity of the TA-like peak. This intensity is correlated to the vibrational bond-bending modes and therefore to the collective vibration of entire Si tetrahedra [31]. Thus a more rigid, or more ordered, network will yield a lower TA-like peak intensity. In order to gain a normalized measure the intensity ratio of the TA-like to the TO-like peak, I_{TA}/I_{TO}, is used with a lower intensity ratio indicating a more ordered network [28, 135, 136]. For this intensity ratio the intensity of the TA-like peak is determined from the maximum on the low-frequency side of the TA-like peak as only this side does not overlap with optic modes [30]. Since the TA-like peak is clearly not Gaussian the maximum intensity of this peak is determined directly from the spectrum after employing the Savitzky-Golay formalism for 5-point smoothing using the package Origin [137]. The intensity of the TO-like peak is analogous to $\Gamma_{TO}/2$ directly determined from the Raman spectrum.

2.2.2 Experimental Details

The Raman spectra, from amorphous as well as crystalline Si, were recorded with a Renishaw 2000 Raman Imaging Microscope using the 632.8 nm excitation line of a helium-neon laser. Spectra were taken using a spot of $\sim$2.0 µm radius, while the incident power was kept below 2.1 mW to avoid laser induced annealing of the samples. An acceptable spectrum was usually obtained after 30 s. Under these testing conditions repeated measurements in the same area confirmed that the a-Si and also the crystalline high-pressure phases were unaltered by the measurement. All peak fitting was performed using the Origin package [137].

2.3 Transmission Electron Microscopy

Extensive use of transmission electron microscopes (TEM) was made throughout this study. Not only conventional TEM and quantitative electron diffraction techniques were used however; such specialist techniques as fluctuation electron microscopy (FEM) and electron-energy-loss spectroscopy (EELS) were also employed. For these various studies samples were prepared in cross-sectional as well as plan-view geometry. Therefore, in this section the various uses of the TEM will be introduced as well as an overview over the sample preparation given.

Simplified, a TEM operates by focusing a beam of electrons through a sufficiently thin (i.e. electron transparent) sample. That beam is then scattered, or diffracted, by the interactions with the sample. This gives localized information about the structure of the sample. For imaging the most common mode of operation is the bright-field mode. For amorphous samples, thicker regions will appear darker, while thinner regions appear brighter due to the contrast formation being solely dependent on the thickness of the film

and the bright-field mean free path Λ_{BF}. Comparing the bright-field intensity $\langle I_{BF}\rangle$ of a uniform area to the intensity of an area of the same size in vacuum $\langle I_0\rangle$ enables thus an estimate of the thickness t by:

$$\frac{\langle I_{BF}\rangle}{\langle I_0\rangle} = exp\left(-\frac{t}{\Lambda_{BF}}\right) \tag{2.11}$$

This convenient means of tracking the sample thickness by normalized bright-field image intensity was used extensively for the FEM experiments in this study.

The TEM used for conventional imaging and selected area diffraction pattern (SADP) analysis was a Philips CM 300 operating at an accelerating voltage of 300 kV. Standard bright-field and dark-field conditions were used. Unless specified otherwise all images and diffraction patterns were taken on negatives and scanned.

One of the major problems of all TEM experiments however, lies in the fact that electron transparent foils need to be prepared from the region of interest. Two different forms of specimen preparation were used in this study. The cross-sectional TEM (XTEM) foils of the residual indent impression were prepared using a focused-ion-beam (FIB) milling system. This was done as positioning with the required sensitivity ($\sim$ 100 nm) is not a straightforward task. Plan-view samples had to be prepared for all the specimens studied for their structural properties. This was necessary as preparation by a FIB leads to implantation-induced amorphization to the foil [102, 138] thus rendering it useless when one wants to investigate the amorphous structure. These two preparation methods will be described in the next section.

2.3.1 Specimen Preparation

Focused-Ion-Beam Milling

A dualbeam FIB system was used for the preparation of the XTEM foils. Such a system uses an SEM for imaging and a gallium ion beam for milling. This is achieved by scanning the Ga^+ beam over the sample in order to sputter away the sample surface. The dualbeam FIB set-up is shown schematically in Fig. 2.8. The electron- and ion-columns are at an angle of 52° to each other allowing the use of both at the same time. During the milling the sample is tilted to 52° to allow ion-beam milling normal to the surface.

The samples of interest are mounted onto an SEM sample holder. In order to ensure precise positioning of the lamella, i.e. the cross-section to be milled, some imaging using the secondary electrons from the Ga^+ beam needs to be performed. Furthermore, the surface can also be damaged by deposition of platinum [138], which is usually performed *in situ* in order to protect the surface. Therefore, prior to inserting the samples into the FIB system, a $\sim$50 nm layer of gold was sputtered onto the surface.

After positioning the desired indent in the middle of the screen, two crosses are milled

on each side of the indent [see Fig. 2.9(a)], which the FIB system uses to relocate the exact position after each milling step. A 1 µm platinum layer is deposited on the surface [see Fig. 2.9(b)] and a trench is milled on either side of the indent [see Fig. 2.9(c)]. The Pt layer is deposited in addition to the Au sputtered onto the sample in order to prevent ion-implantation induced damage to the surface during the milling. After the cross-section is thinned to a thickness of $\sim$1 µm a so-called U-cut is performed, whereby the sample is tilted to 7° which allows the ion beam to free one side and the bottom of the cross-section from the bulk sample [see Fig. 2.9(d)]. Then the cross-section is thinned to its final thickness of $\sim$150 nm. Finally, the second side of the cross-section is freed. The cross-section is then plucked *ex situ* by bringing a sharp glass needle close to the cross-section. Due to electrostatic forces the cross-section will stick to the needle and can be moved onto a TEM grid coated with a carbon membrane.

The dualbeam FIB system used in this study was, unless marked differently, a FEI xT Nova NanoLab 200 FIB located at the Electron Microscope Unit of the University of New South Wales.

Care has to be taken with the TEM specimen preparation when probing for the structural properties of amorphous materials as, for example, further Ga^{+}-induced amorphization of the side walls results from preparation by FIB [138]. Therefore, only specimens for which such further amorphization did not prove a problem were prepared using the FIB system, namely the specimens studied for the occurrence of phase transformation or for possible microstructure such as porosity or nanocrystallinity.

Note that even with the precise positioning possible with a dualbeam FIB system, the

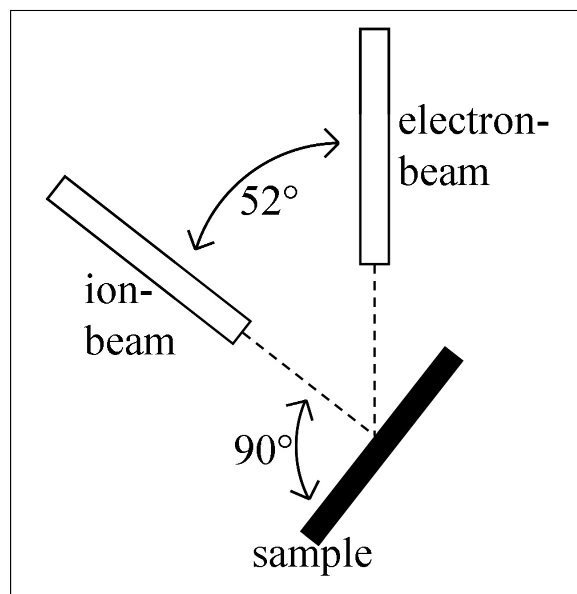

Figure 2.8: Schematic of beam columns and sample configuration in a dualbeam FIB.

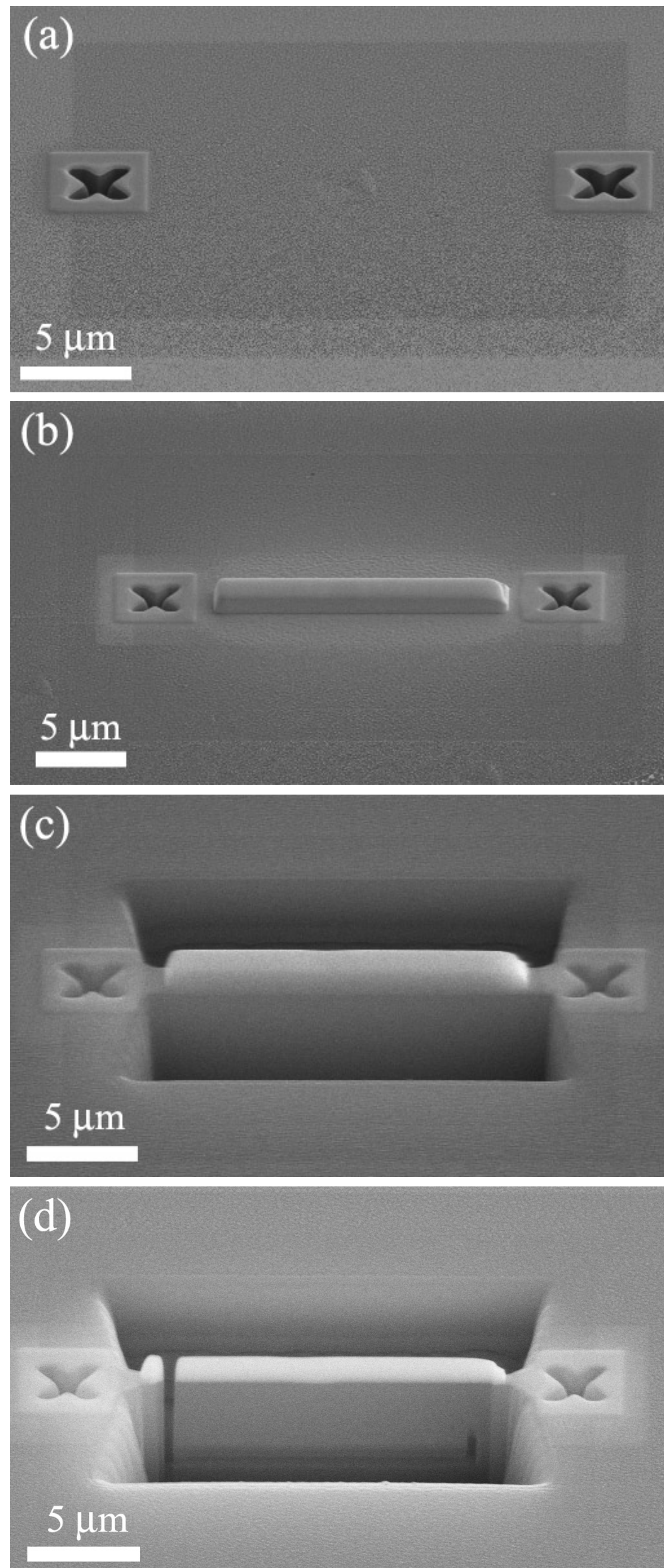

Figure 2.9: Images taken during the milling process in the dualbeam FIB using the high resolution SEM: (a) indent with marker crosses on each side, (b) indent with deposited platinum, (c) thinned cross-section and (d) cross-section after the U-cut is performed.

preparation of residual indents made with the Hysitron TriboIndenter is challenging as these indents are barely visible when imaging with the ion-beam if coated in Au. Therefore, very careful alignment of the FIB had to be performed prior to milling and more often than not, the exact location of a Hysitron indent was determined by correlating other surface features visible on both the electron and ion-beam images.

Plan-View Sample Preparation

The TEM foils made for investigation of the structural properties of a-Si have to be prepared by means which do not result in any modification of the foil during the preparation process. Tripod polishing was not possible as the very small volumes of PI a-Si created by indentation (although relatively large for indentation-scales) were meant to be studied. As preparation by ion-milling with, for example, argon or the use of a FIB is therefore not possible due to amorphization, the TEM foils were prepared by back thinning in plan-view geometry employing a wet-etch technique.

In the case of large-scale a-Si films created by ion-implantation or deposition 3 mm diameter disks were cut using a Gatan Ultrasonic Disc Cutter 601. For the PI a-Si the same sized disks were cut from c-Si. Indentation using the UMIS was then performed in the middle of the 3 mm diameter c-Si samples to make PI a-Si. Sufficient indentations to cover an area of $\sim$400$\times$400 µm^2 were made in order to ensure enough PI a-Si would survive the specimen preparation process.

A portion of all the disks, ion-implanted a-Si, deposited and c-Si disks containing PI a-Si, were then relaxation annealed in a tube furnace prior to any thinning[b]. This was done in order to ensure that structural relaxation could take place as electron transparent a-Si foils are known to behave differently upon annealing [46].

Thereafter, all samples were dimpled to a thickness of $\sim$10 µm using a Gatan Dimple Grinder 656 and then further thinned by wet-etching to electron transperancy using HNO_3:HF:CH_3COOH. A mixture of 5:1:1 was used unless specified otherwise. A bright-field micrograph of an example of such a plan-view specimen made from c-Si disks containing PI a-Si is shown in Fig. 2.10. This particular specimen had been thinned until a small hole appeared in the centre of the specimen visible on the lower right of the image. Some of the residual indent impressions containing PI a-Si are marked with arrows. Clearly, the a-Si etched faster than the surrounding c-Si matrix. Therefore, indents further away from the central hole proved best for further TEM investigation.

In order to overcome problems with the different etch-rates of the PI a-Si and the c-Si matrix, etching with KOH had been tried. This proved impossible however, as the PI a-Si etched slower than the surrounding c-Si matrix resulting in PI a-Si no longer being connected to the rest of the sample. Furthermore, the HNO_3:HF:CH_3COOH etching had to

[b]For details on the furnace annealing refer to the next chapter, Section 3.6.

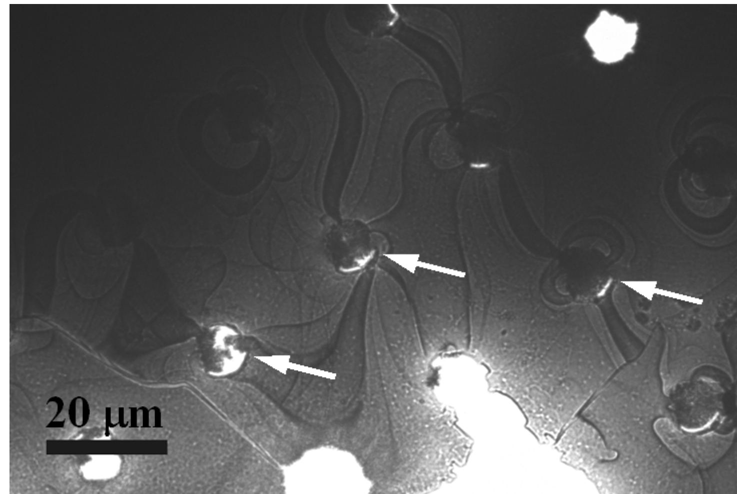

Figure 2.10: Low magnification bright-field image of a plan-view TEM specimen prepared from indentations. Note that the image was taken with a CCD camera in the IVEM Hitachi located at Argonne National Laboratory.

be performed very carefully, as a too slow etch-rate of the a-Si resulted in crystallization of some of the films, especially of the as-indented PI a-Si. A too fast etch-rate, however, resulted in surfaces too rough for FEM investigation which requires a 250×250 nm^2 uniform area.

Therefore, the best results were obtained by making a large number of such samples and then checking them very carefully for their amorphicity. In some cases it even proved necessary to re-check the same sample in another microscope as, for example, the instrument used for the first FEM study was a dedicated high-resolution instrument and thus less optimal for relative low magnification investigation. An example of such a foil which appeared at first amorphous is shown in Fig. B.1 in Appendix B, Section B.1. However, etch-induced crystallization was not the only problem which warranted preparation of a large number of samples. The plan-view samples proved extremely brittle and, especially the c-Si disks containing the PI a-Si, sometimes shattered simply by touching them with tweezers. Therefore, a large number of samples proved the best way of performing an extensive study.

Specimens prepared in this manner were used for all structural studies performed by TEM, i.e. for studies by electron diffraction, FEM and EELS. These techniques are now described in detail.

2.3.2 Electron Diffraction

Electron diffraction is extremely useful when one wants to study the structure of amorphous materials, especially of small volumes. Only electrons can be focused down to illuminate nanovolumes and thus allow insight into their structure [24], making electron

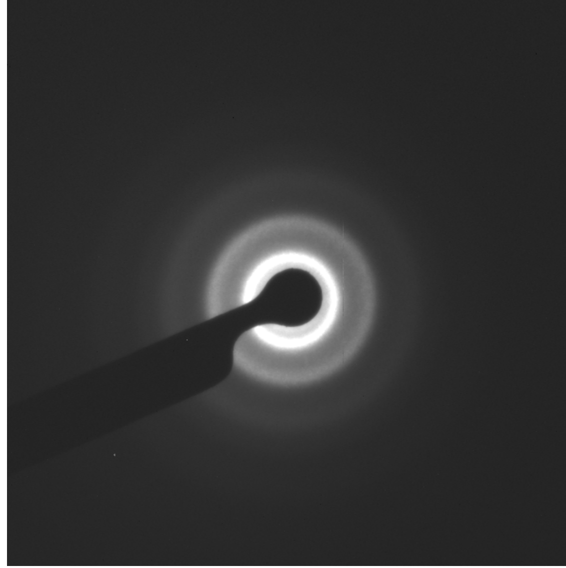

Figure 2.11: Example of a diffraction pattern from amorphous silicon.

diffraction ideal for examining the small volumes of PI a-Si made by indentation.

From such a diffraction experiment of an amorphous material one usually obtains the radial distribution function (RDF) or $J(r)$. This RDF is related to the 2-body or pair distribution function (PDF), $g_2(\mathbf{r}_{1,2})$, which describes the probability of finding a second atom at a distance $\mathbf{r}_2$ from the first atom at $\mathbf{r}_1$ averaged over all atoms in the volume. In a homogeneous, isotropic system this PDF can be replaced by $g(r)$ for $r = |\mathbf{r}| = |\mathbf{r}_1 - \mathbf{r}_2|$, which is then directly related to the local density at a distance r from an arbitrary central atom. With the origin located on an atom, the average number of atoms in a spherical shell of thickness dr at a distance of r can be calculated to be:

$$\int_{shell} n_0 g(r) dr = 4\pi r^2 n_0 g(r) dr = n_0 J(r) dr, \tag{2.12}$$

whereby $n_0 = N/V$ is the average number of atoms N in the volume V and $J(r) = 4\pi r^2 g(r)$.

Another very important parameter in electron diffraction is the reduced RDF $G(r)$, which is related to $J(r)$ by:

$$J(r) = rG(r) + 4\pi r^2 \rho_0. \tag{2.13}$$

Therein ρ_0 is the macroscopic mass density and thus $G(r)$ oscillates about the r-axis. Additionally, the regime between the origin and the first peak follows the line $G(r) = -4\pi r \rho_0$.

An example of a typical diffraction pattern obtained from electron diffraction of a-Si is shown in Fig. 2.11. After carefully excluding the area covered by the beam stop, the diffracted intensity is calculated by azimuthal averaging. In order to then obtain the

above mentioned functions from this diffraction pattern the scattered intensity needs to be considered in detail.

A monatomic, isotropic amorphous material like a-Si yields for the scattered amplitude $A(\mathbf{k})$ in direction $\mathbf{k}$ from an atom i at $\mathbf{r}_i$:

$$A(\mathbf{k}) = f_i(\mathbf{k}) exp(i\mathbf{k} \cdot \mathbf{r}_i), \tag{2.14}$$

where $f_i(k)$ is the atomic scattering factor, and $k = |\mathbf{k}| = 4\pi sin(\theta)/\lambda$ with the scattering angle 2θ and the wavelength λ of the scattered radiation. As $g(r)$ is directly related to the local average density, one can integrate over the sample volume and the scattered intensity $I(k)$ can be calculated according to the Debye formula [139]. Additionally neglecting the influence of small scattering angles and considering a particular $r = |\mathbf{r}_i - \mathbf{r}_j|$ yields:

$$I(k) = Nf^2(k) + 4\pi Nf^2(k) \int_0^\infty [g(r) - \rho_0] \frac{r}{k} sin(kr) dr. \tag{2.15}$$

In this equation, the first term arises from atoms scattering independently, whereas the second term causes a deviation from this mean intensity if the local density at r deviates from ρ_0. To then extract $g(r)$ the reduced intensity function $\phi(k)$ is used in electron diffraction:

$$\phi(k) = \left[\frac{I(k) - Nf^2(k)}{Nf^2(k)} \right] k. \tag{2.16}$$

From $\phi(k)$ the sought functions $g(r)$, $G(r)$ and $J(r)$ can be obtained by Fourier transformation and mathematical manipulation:

$$G(r) = 4 \int_0^\infty \phi(k) sin(kr) dk = 4\pi r[g(r) - \rho_0] = J(r)/r - 4\pi r \rho_0. \tag{2.17}$$

For further details on the theory and technical details refer for example to Refs. [24, 140] and references therein.

These functions yield significant insight into the structure of the amorphous material studied such as mean bond-length, mean bond-angle and coordination number. For example, the mean bond-length is equivalent to the position of the first peak r_1 of $G(r)$ or $J(r)$. Furthermore, the width of this first peak is correlated to the spread in bond-length.

Moreover, the coordination number (CN) can be directly determined from $J(r)$, since $J(r)$ is scaled with the mass density ρ_0. Therefore, the area under the first peak represents all first-nearest neighbours (i.e. the probability of finding any atoms at a first-nearest neighbour distance). Usually integration of the area under the first peak of $J(r)$ within some limits on r on either side of the peak yields the CN. However, X-ray diffraction studies [14] have also obtained CN from the area of a Gaussian fitted to this first peak rather than from integration.

Additionally, the mean bond-angle $\overline{\theta}$ can be calculated from the peak positions of the first and second peak r_2 in the RDF by:

$$\overline{\theta} = arccos\left(\frac{2r_1^2 - r_2^2}{2r_1^2}\right). \tag{2.18}$$

Furthermore, the static disorder width $\Delta\theta_G$ can be obtained from the width of a Gaussian fitted to the second peak of the RDF [12]. From $\overline{\theta}$ and $\Delta\theta_G$ the bond-angle distortion $\Delta\theta$, which is also measurable by Raman microspectroscopy, can be calculated by [141]:

$$(\Delta\theta)^2 = (\Delta\theta_G)^2 + (\theta_t - \overline{\theta})^2 \tag{2.19}$$

with the ideal tetrahedral angle θ_t of 109.45°.

Experimental Details

The electron diffraction study was performed in collaboration with the University of Oxford. The experiment was performed on a Jeol JEM-3000F FEGTEM. The SADPs were collected with a CCD camera. During each session an additional diffraction pattern of c-Si was taken for accurate calibration of the reciprocal space recorded. No energy filtering was used, as energy filtering for very thin foils introduces more experimental problems than the results warrant such as nonlinearities in the data collection or a low energy dispersion across the diffraction pattern [24]. In order to minimize the effect of multiple scattering the foils were kept thin at a few nm thickness. Since Si is well known to grow a layer of native oxide of $\sim$1 nm on the surface, the oxide was stripped off immediately prior to the TEM investigation. This was achieved by etching the specimens in a HF:H_2O mixture for a few seconds. Note that no longer etching time was possible as the etchant tended to crystallize the very thin a-Si films. After collection, the SADPs were azimuthally averaged and normalization of the intensity $I(k)$ was performed[c] in order to obtain $\phi(k)$. The $\phi(k)$ was cut-off at $2\pi \times 2.5$ Å^{-1} for all samples as some areas proved too noisy beyond this point. $G(r)$ was then obtained by a Fourier transform whereby a damping factor of 0.16 was applied in order to dampen the high-oscillation noise. Approximately 5 areas were used for each form of a-Si for the consequent analysis. The results presented are always the average of these 5 areas with the error being the standard error.

2.3.3 Fluctuation Electron Microscopy

As powerful a technique as electron diffraction proves to be, no structure is visible beyond $\sim$8 Å as pair correlations average out at larger r due to the disorder. This however,

[c]The normalization was performed according to the procedure established at the University of Oxford by Y. Chen, G. Li and D. J. H. Cockayne.

does not mean that no structure beyond this scale is present. Attempts to study this so-called medium-range order (MRO) have been made by high-resolution TEM methods (see Ref. [45] and references therein). However, this proved very problematic due to uncertainties in the image interpretation and even more due to the fallibility of the human eye which tends to see patterns where none exist. Fluctuation electron microscopy (FEM) overcomes these problems by being a low-resolution technique based on statistical analysis. This technique is described in this section.

FEM detects MRO in amorphous materials by investigating spatial fluctuations in coherent scattering. These fluctuations in the diffracted intensity appear as speckle in images as well as diffraction patterns. Examples of such dark-field images and nanodiffraction patterns are shown in Fig. 2.12.

It would be easy to conclude that these speckles of bright and dark spots correspond to volumes of Bragg-diffracting ordered regions, i.e. bright spots diffract strongly and dark spots diffract weakly. However, speckle can also arise from coherent diffraction of random atomic alignments and thus, the presence of speckle does not necessarily prove the presence of Bragg-diffracting ordered regions. In order to distinguish the MRO reliably against this background of random speckle, statistical methods are used. Therefore, the speckle is quantified by determining the variance of the image intensity. With the aperture radius Q and the scattering vector $\mathbf{k}$ this variance is calculated from the dark-field image intensity $I(k,Q)$ by:

$$V(k,Q) = \frac{\langle I^2(k,Q)\rangle}{\langle I(k,Q)\rangle^2} - 1, \tag{2.20}$$

where $\langle\rangle$ indicates averaging over the image and $k = |\mathbf{k}| = 4\pi sin(\theta)/\lambda$ as before. The normalization needs to be performed in order to eliminate the intensity drop-off of the atomic form factor with k. With this statistical approach the fallibility of the human eye

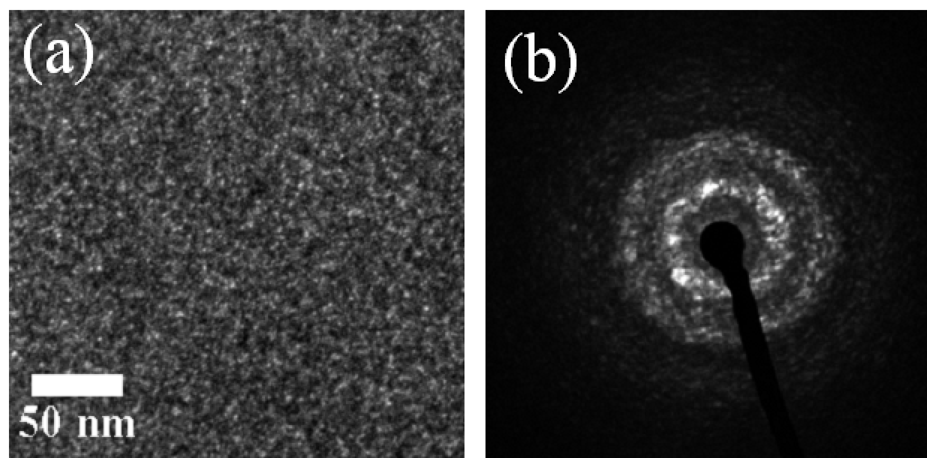

Figure 2.12: Examples of the speckle visible in (a) dark-field images (example taken at a k of 0.32 Å^{-1}) and (b) nanodiffraction patterns of a-Si.

is avoided during the analysis and the speckliness of an image can be quantified. This $V(k, Q)$ is sensitive to the MRO as speckle from a random atomic alignment is not expected to depend on the scattering angle. If a sample consists however, of randomly oriented small clusters, some of them will be oriented in a way to satisfy the Bragg condition and will hence result in a bright spot, whereas others will not diffract and thus appear as dark spots. Therefore, the dark-field image taken from such a more ordered sample will have a high normalized variance. Thus, in general a high degree of variance can be interpreted as a high degree of order (or large amount of structure) and a low degree of variance as a low degree of order.

It has been noted by Jungk *et al.* [142] however, that the $V(k)$ characteristics obtained by FEM appeared to yield similar information as already $I(k)$ obtained by conventional diffraction techniques did. These similarities observed for their samples raised some doubt whether the four-body correlation function can indeed be accessed by FEM. However, a later report [143] gave explicit examples for samples with very different $V(k)$ and $I(k)$ signals. In addition, it was pointed out that Jungk *et al.* [142] had used excessively high image resolution which prevented the detection of diffraction fluctuations in their case.

This dependence of $V(k, Q)$ on the MRO is due to the measurement of $I^2(k, Q)$ rather than $I(k, Q)$ as studied by diffraction techniques. $\langle I(k, Q)\rangle$ is the total diffraction intensity accepted by the objective aperature averaged over the image area and thus depends only on the pair-distribution function $g_2(\mathbf{r}_{12})$ [144]. In contrast, $\langle I^2(k, Q)\rangle$ depends on the four-body correlation function $g_4(\mathbf{r}_{12}, \mathbf{r}_{13}, \mathbf{r}_{14})$, since the 'speckliness' is maximized when similar atom pairs are localized within the same column [144]. Thus, $g_4(\mathbf{r}_{12}, \mathbf{r}_{13}, \mathbf{r}_{14})$ can be thought of as a pair-pair distribution function in which $\mathbf{r}_{12}$ defines a pair of atoms, $\mathbf{r}_{13}$ defines another pair, and $\mathbf{r}_{14}$ is the separation between the two pairs. Due to the isotropy of a-Si this can be simplified to the pair separation r_1, another pair separation r_2, a pair-pair separation r and a relative angle between the pairs θ [50].

Thus, analogous to $g_2(r)$, which searches for atoms in a set of concentric spheres around the atom at the origin, $g_4(r_1, r_2, r, \theta)$ searches in concentric spheres for a pair of atoms with the separation r_2 and a relative angle θ. This additional selectivity means that $g_4(r_1, r_2, r, \theta)$ retains useful information about the structure at significantly greater length-scales than $g_2(r)$ does. As $V(k, Q)$ depends on this $g_4(r_1, r_2, r, \theta)$ albeit heavily filtered and integrated, it also contains information about the MRO.

The dependence of $V(k)$ on this pair-pair distribution function can be illustrated when the numerator (the speckle) and denominator (the square of the total diffracted intensity) in Eq. 2.20 are considered in the kinematical scattering theory. For example, arrangement of two atom pairs in different coherence volumes will result in less non-zero 'diffraction' terms than in non-zero 'speckle' terms. In contrast, placing two such pairs into different Airy discs will not change the number of non-zero 'diffraction' terms, but will half the

number of non-zero ‘speckle’ terms. Thus the image variance is sensitive to pair-pair correlations, whereas the mean image intensity (the diffracted intensity) is limited to the pair correlation. For further details see Ref. [144].

The Different Methods of Fluctuation Electron Microscopy

Two principle methods of FEM can be used, the *variable coherence* microscopy where k is systematically varied at a constant Q and the *variable resolution* microscopy where Q is varied at a constant k. In a TEM the first method is significantly easier as k can simply be changed electronically, whereas Q has to be changed manually. This is different however, in a scanning transmission electron microscope (STEM) where Q can be varied without any problems. Both, TEM and STEM can yield the same results as the geometry is essentially equivalent. This is shown schematically in Fig. 2.13.

In a tilted dark-field TEM the incident electron wave of wavelength λ and amplitude $\chi = 2\theta/\lambda$ is inclined to the optic axis by k. This corresponds to an illumination tilt angle of $sin(|\mathbf{q}|/\chi)$, which approximates to $|\mathbf{q}|/\chi$ for small $|\mathbf{q}|$. The radiation is scattered by the object into an outgoing plane wave that is inclined to the optic axis by an amount q. In the convention used in the schematic the condition $k = q$ corresponds to no scattering

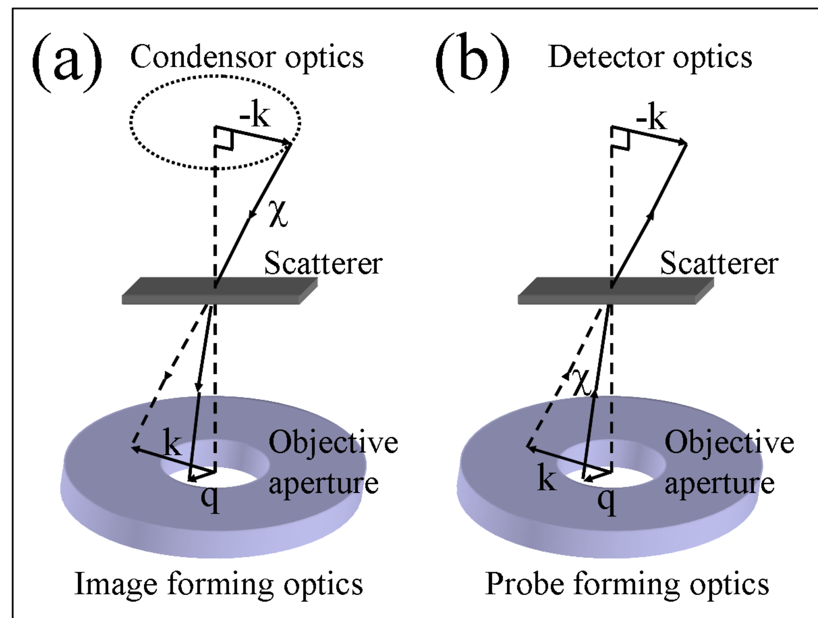

Figure 2.13: Simplified schematic of the reciprocal equivalency of the scattering geometry according to Treacy *et al.* [45]. (a) In a conventional TEM the electron beam enters through the condenser system and the image resulting from the scattering of the sample is collected after the objective aperture. (b) In a STEM the probe is formed by the objective aperture and the scattering is then collected by detectors.

of the incident beam and q and k are related to real-space spacings d through $k = 2\pi/d$. In this geometry the diffraction vector k is fixed and the data are collected as dark-field images with intensity varying with position r, i.e. data are collected as $I(k_{fixed}, r)$. In a STEM where only a small volume of the sample is probed at a time and nanodiffraction patterns are collected at each point, the data are collected as $I(k, r_{fixed})$. Therefore, the speckle statistics of these nanodiffraction patterns are analysed rather than dark-field images. If the TEM scans all k and the STEM all r, the two data sets are in principle identical. In practice however, FEM by STEM nanodiffraction involves fewer spatial samples than FEM by TEM which means that the noise will be a greater problem than in a TEM. Nonetheless, the more efficient use of the diffracted electrons allows much denser sampling in k at lower sample dose than possible in a TEM [145]. Moreover, investigation of the intensity at high k of individual nanodiffraction patterns allows for corrections of thickness variations across the sampled volume[d].

For further details on the technique of FEM refer to Refs. [45, 50] and references therein and for in-depth information on STEM-FEM refer to Refs. [145, 146].

Interpretation of Fluctuation Electron Microscopy Data

One of the major problems of FEM however, is that FEM data cannot be readily inverted. Therefore, structural information is usually inferred from simulations of structural models. As detailed in Chapter 1 two principally different models have been found to date, a paracrystalline model [15, 47, 50, 51, 147, 148] and a void model [53, 54].

Nonetheless, significant information can be concluded from the FEM data without the need for modelling. For example, for the case of amorphous semiconductors the magnitude of the variance has been correlated with the degree of MRO by interpreting a higher variance as indicative of a higher degree of MRO [47, 48, 55, 149]. This degree of MRO depends on a number of indistinguishable factors such as the number of regions of correlated structure, the size of these regions and the relative order within such a region. Moreover, the positions of the peaks in the variance plot give some additional insight into the local bonding and the type of MRO within the regions of correlated structure [45, 150].

Another interesting feature of the FEM data is the peak magnitude ratio of the second to first (and also third to second) peaks. The first peak is correlated to diffraction from the $\{111\}$ planes, whereas the second peak corresponds to the $\{220\}$ planes. It has been shown that diffraction from the $\{220\}$ planes is more sensitive to changes in MRO than the diffraction from the $\{111\}$ planes [15]. Therefore, changes in the peak magnitude ratio can indicate significant differences in MRO. For example, the shape as well as the size of the ordered regions plays a role in determining the peak magnitude ratios [151]. Furthermore, simulations from various paracrystalline models (CRNs containing a vary-

[d]This correction of thickness variations has been implemented and standardized by S. Bogle at the University of Illinois at Urbana-Champaign.

ing number of paracrystals of varying sizes) have shown that the peak magnitude ratio varies linearly as a function of paracrystallite diameter [152]. However, care has to be taken when investigating the peak magnitude ratio as a thickness gradient over the sample area studied may also result in an increased peak magnitude of the second over the first peak[e]. Therefore, in this study only data obtained from STEM-FEM with its increased resolution in k and capability for roughness correction will be investigated for this peak magnitude ratio.

Interestingly, the MRO measured by FEM has also been directly correlated to characteristics of the structural order obtained from Raman microspectroscopy. An experimental study [153] on the influence of low-energy bombardment of sputtered a-Si observed an increase in the MRO as determined by FEM with increasing ion/neutral flux ratio. This increase was accompanied by an increase in the intensity ratio of the longitudinal optic (LO)-like peak to the transverse optic (TO)-like peak obtained by Raman microspectroscopy. A further study [147] employed molecular-dynamics to simulate the FEM signal as well as Raman spectra of paracrystalline networks. They observed a decrease in the intensity ratio of the transverse acoustic (TA)-like to TO-like peak with increasing grain size of the paracrystallites. However, it should be noted that a model of a continuous random network created by the same algorithm yielded an even lower intensity ratio [30]. In addition, relaxed implanted a-Si is known to exhibit the lowest intensity ratio observed to date [28]. Therefore, care has to be taken when correlating a low intensity ratio to a large paracrystal sizes as a well ordered amorphous network can yield a similarly low ratio.

Experimental Details

Two different methods of FEM were used in this study, the tilted dark-field method and FEM based on nanodiffraction.

The first set of experiments using the tilted dark-field method was performed in collaboration with Argonne National Laboratory. For this experiment a Jeol JEM-4000EXII operating at 200 keV to avoid damage by the electron beam was used. The FEM consisted of the automated acquisition of a series of tilted dark-field images at different incident beam tilts. The hollow-cone dark-field TEM technique that is more commonly employed for FEM is the incoherent azimuthal average of the tilted dark-field technique and probes essentially the same structural information [45, 150]. The images were filtered to remove distortions and noise and the normalized intensity variance was calculated [150]. The size of the objective aperture dictates a sensitivity to the MRO up to 1.2 nm in extent. The intensity variance is presented as a function of the incident beam tilt projected onto the diffraction plane, k [Å^{-1}]. The size of the dark-field images was 250×250 nm^2. To avoid thickness effects [150], only areas of a uniform thickness of $\sim$50 nm were studied in all

[e]This has been demonstrated explicitly by S. Bogle on one of the back thinned a-Si specimen with a steep thickness gradient in a private communication.

specimens. This thickness was estimated and controlled by measuring the normalized bright-field image intensity according to Eq. 2.11. Approximately 10 dark-field series' were obtained from different areas of each specimen. The displayed FEM data is the average of the 10 measurements and the uncertainty is the standard error.

The second set of experiments was performed in collaboration with the University of Illinois at Urbana-Champaign. This experiment was performed on a STEM collecting nanodiffraction patterns rather than dark-field images. A Jeol 2200FS with a Schottky field emission gun was used for this study. A condenser aperture of 30 μm diameter was used to define a probe of 1.6 nm size. The condenser deflectors were used to scan a square grid of at least 10×10 points with at least 10 nm spacing in between. A nanodiffraction pattern was collected at each point with the CCD camera. For each sample five areas or more were scanned for a total of at least 500 nanodiffraction patterns. The $V(k)$ characteristics were calculated by first azimuthally averaging each pattern to get $I(k)$, the intensity as a function of the magnitude of the scattering vector, and by then computing the variance for each area. For further experimental details see Ref. [146]. To avoid thickness effects only areas of a uniform thickness were studied in all specimens, which was again controlled by measuring the normalized bright-field image intensity. Additionally, the individual areas were corrected for roughness and thickness variations by checking $I(k)$ of each nanodiffraction pattern at high k for aberrations in $I(k)$. Such aberrations in intensity are indicative of thickness variations thus allowing for filtering of non-uniform thickness. The displayed FEM data is the average of the five or more areas measured and the uncertainty is the standard error.

2.3.4 Electron-Energy-Loss Spectroscopy

Electron-energy-loss spectroscopy (EELS) was used to measure the mass density of various forms of a-Si. EELS measures the energy distribution of electrons that have interacted inelastically with the sample, i.e. as the name says the energy-loss. However, in a typical spectrum recorded with a special EELS detector not only the inelastic, also the elastic scattering is detected. Therefore, the resulting spectrum can be separated into three principal regions: the zero-loss, the low-loss and the core-loss. The zero-loss consists of the elastically forward-scattered electrons and is used for calibration of the spectrum. The low-loss region contains information about the interaction of electrons with the outer-shell electrons of the atoms. Lastly, the core-loss (or high-loss) region reveals information about interaction of the electrons with the inner-shell electrons and thus about the atoms in the sample. In this present study however, only the low-loss spectrum was analysed and therefore, only this regime will be discussed below.

An example of a low-loss spectrum of a-Si is shown in Fig. 2.14. The first peak is the zero-loss peak with the intensity I_0 and the second peak is the plasmon peak with the

intensity I_p and its position at the plasmon-energy E_p, the energy lost by an electron when it generates a plasmon. The low-loss spectrum is proportional to the energy-loss function, $Im(-1/\epsilon(E))$, with the complex dielectric function $\epsilon(E)$. In the free-electron limit $\epsilon(E)$ is given by the Drude model:

$$\epsilon(E) = 1 - \frac{E_p^2}{E^2 + iE\Gamma}, \tag{2.21}$$

whereby Γ is the full-width at half-maximum of the plasmon-peak and E_p the plasmon-energy:

$$E_p = \hbar \left(\frac{n_e e^2}{\epsilon_0 m^*} \right)^{1/2}, \tag{2.22}$$

with the valence electron density n_e the vacuum dielectric function ϵ_0 and the electron 'effective mass' m^* (m being the free-electron mass). This yields for the energy-loss function:

$$Im\left(\frac{-1}{\epsilon(E)}\right) = \frac{E_p^2 E\Gamma}{(E^2 - E_p^2)^2 + (E\Gamma)^2}. \tag{2.23}$$

For further details see for example Ref. [154].

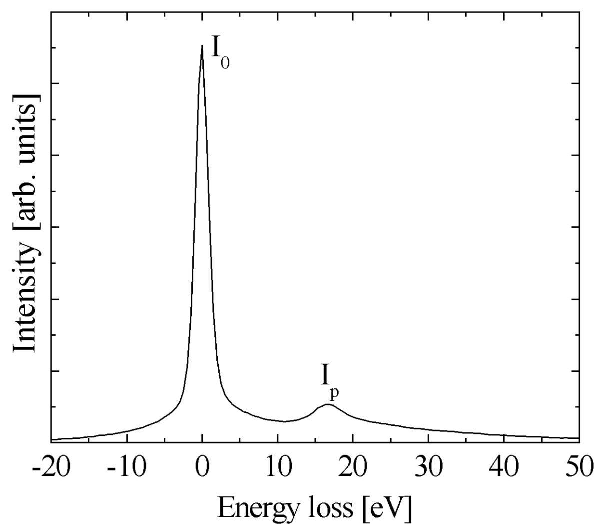

Figure 2.14: Example of the low-loss spectrum taken from as-indented PI a-Si. The low-loss region displays the zero-loss peak and the first plasmon peak at ~16.7 eV.

Determination of the Mass Density

The valence electron density can be used to derive the mass density as has been shown by Ferrari *et al.* for carbon [155]. Equivalently, the mass density of silicon can be derived by assuming that each silicon atom contributes 4 valence electrons:

$$n_e = 28\frac{\rho_0 N_A}{M_{Si}}\left(\frac{4X_{Si}}{28X_{Si}}\right), \tag{2.24}$$

whereby N_A is the Avogadro constant, M_{Si} is the atomic mass of silicon and X_{Si} is the silicon fraction. This equation is displayed in an equivalent way to the original equation (27) in Ref. [155]. Combining this equations above with the plasmon-energy, the mass density of crystalline and amorphous silicon is given by:

$$\rho_0 = \frac{\epsilon_0}{4\hbar^2 N_A e^2} M_{Si} m^* E_p^2 \tag{2.25}$$

There are only two unknowns in Eq. 2.25, the plasmon energy E_p and the effective electron mass m^*. The effective electron mass arises from the assumption of a 'quasifree' electron model for the valence electrons. It is well known for c-Si, but not for pure a-Si. However, theoretical calculations have shown that a crystalline material and its amorphous counterpart have an equivalent m^* [156]. Thus, the longitudinal m^* of 0.98 [157] was assumed for all 5 types of materials studied by EELS: c-Si, as-prepared and relaxed ion-implanted and PI a-Si. Additionally, it was assumed that all five materials contribute the same 4 valence electrons per atom.

Experimental Details

The EELS was also performed in collaboration with Argonne National Laboratory. The parallel electron-energy-loss spectroscopy was performed in a Philips CM30T operating at 100 keV using a Gatan 666 parallel electron-energy-loss (PEEL) spectrometer. PEEL spectra were recorded in diffraction mode using convergence and collection semiangles of 3 and 5 mrad, respectively. Five areas were measured per sample type. The thicknesses of these areas were estimated from the low-loss spectrum using Digital Micrograph EELS analysis [158] and were estimated to be $\sim$20-40 nm.

The plasmon-energy was then determined from the low-loss spectrum after de-convolution of the plasmon peak from the zero-loss peak. The de-convolution was carried out on the calibrated spectra using Digital Micrograph EELS analysis [158] and was performed using the Fourier-Log option and a Gaussian-Lorentz fit to the zero-loss peak[f]. Although the presence or absence of the L-edge of the core-loss spectrum did not seem to influence the region of the plasmon peak, the spectra were truncated to avoid inter-

[f]It had also been attempted to de-convolute the data by the Richardson-Lucy algorithm by R. Arenal which proved not successful due to too low intensity of the data.

ference. The thus obtained single-scattered spectra were fitted employing the non-linear least-squares curve fitting routine MPFIT for IDL [159]. Fitting with either a Gaussian or a Lorentzian resulted in under-estimation of the mass density, whereas fitting explicitly with the energy-loss-function stated in Eq. 2.23 and a baseline, resulted in over-estimation of the mass densities as the baseline compensated for the presence of the surface excitations. Therefore, the fitting was performed with a DC offset and the energy-loss-function. Although this resulted in slightly poorer fits in terms of reduced χ^2 than the other fits, it also resulted in mass density values that matched literature values for known forms of a-Si.

The results presented are the averages from the five areas measured for each specimen and the error denoted is the standard error.